

AD\_\_\_\_\_

Award Number: W81XWH-08-1-0701

TITLE: Micro and Nano-mediated 3D Cardiac Tissue Engineering

PRINCIPAL INVESTIGATOR: Rashid Bashir, Ph.D.

CONTRACTING ORGANIZATION: University of Illinois at Urbana-Champaign  
Urbana, IL 61801

REPORT DATE: September 2012

TYPE OF REPORT: Annual

PREPARED FOR: U.S. Army Medical Research and Materiel Command  
Fort Detrick, Maryland 21702-5012

DISTRIBUTION STATEMENT: Approved for Public Release;  
Distribution Unlimited

The views, opinions and/or findings contained in this report are those of the author(s) and should not be construed as an official Department of the Army position, policy or decision unless so designated by other documentation.

REPORT DOCUMENTATION PAGE				Form Approved OMB No. 0704-0188	
Public reporting burden for this collection of information is estimated to average 1 hour per response, including the time for reviewing instructions, searching existing data sources, gathering and maintaining the data needed, and completing and reviewing this collection of information. Send comments regarding this burden estimate or any other aspect of this collection of information, including suggestions for reducing this burden to Department of Defense, Washington Headquarters Services, Directorate for Information Operations and Reports (0704-0188), 1215 Jefferson Davis Highway, Suite 1204, Arlington, VA 22202-4302. Respondents should be aware that notwithstanding any other provision of law, no person shall be subject to any penalty for failing to comply with a collection of information if it does not display a currently valid OMB control number. <b>PLEASE DO NOT RETURN YOUR FORM TO THE ABOVE ADDRESS.</b>					
1. REPORT DATE September 2012		2. REPORT TYPE Annual		3. DATES COVERED 24 September 2011 – 15 August 2012	
4. TITLE AND SUBTITLE  Micro and Nano-mediated 3D Cardiac Tissue Engineering				5a. CONTRACT NUMBER	
				5b. GRANT NUMBER W81XWH-08-1-0701	
				5c. PROGRAM ELEMENT NUMBER	
6. AUTHOR(S)  Rashid Bashir, Ph.D. Brian Cunningham, Ph.D., Hyunjoon Kong, Ph.D., Taher Saif, Ph.D., and Larry Schook, Ph.D. E-Mail: rbashir@illinois.edu				5d. PROJECT NUMBER	
				5e. TASK NUMBER	
				5f. WORK UNIT NUMBER	
7. PERFORMING ORGANIZATION NAME(S) AND ADDRESS(ES)  University of Illinois at Urbana-Champaign Urbana, IL 61801				8. PERFORMING ORGANIZATION REPORT NUMBER	
9. SPONSORING / MONITORING AGENCY NAME(S) AND ADDRESS(ES) U.S. Army Medical Research and Materiel Command Fort Detrick, Maryland 21702-5012				10. SPONSOR/MONITOR'S ACRONYM(S)	
				11. SPONSOR/MONITOR'S REPORT NUMBER(S)	
12. DISTRIBUTION / AVAILABILITY STATEMENT Approved for Public Release; Distribution Unlimited					
13. SUPPLEMENTARY NOTES					
14. ABSTRACT  The project envisages to improve the care of battlefield-related cardiac injuries by providing novel methods to design and fabricate 3-D models of cardiac sub-components that would be critical in restoring the function of the heart. We report the integration of dielectrophoresis (DEP) with stereolithography (SL) apparatus for the spatial patterning of cells on custom made gold micro-electrodes. We showed the patterning and encapsulation of mouse embryonic stem cells and skeletal muscle myoblasts. A robust and flexible in vitro platform was developed for stem cell differentiation and tissue engineering, by mimicking elements of the native 3D in vivo cellular micro-environment. It was shown that a sequential drug delivery can be attained with the hydrogel created in this study, and that the sequential delivery of two complementary proangiogenic factors can significantly increase vascular density in a target tissue. To test hydrogel constructs in vivo we developed a mouse myocardial infarction model. We demonstrated several new capabilities of photonic crystal biosensors using photonic crystal enhanced microscopy (PCEM), enabling visualizing of dynamic cell attachment at much higher resolution and sensitivity for highly detailed quantification of attachment distribution within individual cells. This provides a novel tool for the study of cell attachment for various applications, including wound healing, cell culture optimization, stem cell differentiation, and cancer metastasis.					
15. SUBJECT TERMS Biomaterials, Biosensors, Fabrication, Mechanobiology					
16. SECURITY CLASSIFICATION OF:			17. LIMITATION OF ABSTRACT	18. NUMBER OF PAGES	19a. NAME OF RESPONSIBLE PERSON
a. REPORT	b. ABSTRACT	c. THIS PAGE			USAMRMC
U	U	U	UU	67	19b. TELEPHONE NUMBER (include area code)



**nano@illinois**<sup>TM</sup>  
*nano solutions for mega problems*

# ANNUAL REPORT

**2011-12**

## **Micro and Nano-mediated 3D Cardiac Tissue Engineering**

**Rashid Bashir, PI**  
**University of Illinois**  
[rbashir@illinois.edu](mailto:rbashir@illinois.edu)

**Submitted: November 27, 2012**

Micro and Nanotechnology Laboratory  
Center for Nanoscale Science and Technology\*  
Institute for Genomic Biology  
[www.illinois.edu](http://www.illinois.edu)

*\*The US Army TATRC-funded Micro and Nano-mediated 3D Cardiac Tissue Engineering is a project of the University of Illinois Center for Nanoscale Science and Technology (CNST) collaboration*

## **Table of Contents**

### **Contents**

I. SUMMARY OF WORK.....	5
II. INTRODUCTION .....	5
III. BODY .....	7
IV. KEY RESEARCH ACCOMPLISHMENTS .....	7
V. REPORTABLE OUTCOMES.....	8
VI. CONCLUSION .....	9
SECTION II: Annual Report from Project Subgroups.....	10
Research Group: Rashid Bashir .....	10
Research Group: Taher Saif.....	13
Research Group: Larry Schook .....	14
Research Group: Hyunjoon Kong.....	18
Research Group: Brian Cunningham .....	21

## **Annual Report (Rashid Bashir)**

1. Award No. Army W81XWH-08-1-0701
2. Report Date: November 27, 2012
3. Reporting period: 2011-12
4. Principal Investigator: Rashid Bashir, University of Illinois
5. Telephone No.: 217-333-3097
6. Award Organization: University of Illinois
7. Project Title: **Micro and Nano-mediated 3D Cardiac Tissue Engineering**
8. Current staff, role and percent effort of each on project.

	<b>Role</b>	<b>% Effort</b>
Rashid Bashir	PI	2%
Brian Cunningham	Co-PI	2%
Hyunjoon Kong	Co-PI	2%
Taher Saif	Co-PI	2%
Larry Schook	Co-PI	2%
Jae Hyun Jeong	Postdoc Assoc.	100%
De Souza, Emerson	Postdoc Assoc.	100%
P. Bajaj	Graduate Res. Assistant	50%

**Army W81XWH-08-1-0701**

**Project Duration: 2008 - 2012**

**Total Award -**

**Award Expenditures: September 24, 2008 to September 30, 2012**

<b>COST ELEMENTS</b>	
Personnel	
Fringe Benefits	
Supplies	
Equipment	
Travel	
Other Direct Costs	
<b>Subtotal</b>	
Indirect Costs	
Fees	
<b>Total</b>	

**Research Groups**

- I.** Rashid Bashir, PI
- II.** Taher Saif, co-PI
- III.** Larry Schook, co-PI
- IV.** Hyun Joon Kong, co-PI
- V.** Brian Cunningham, co-PI

## SECTION I: Annual Report Overall Project

This section describes briefly the salient aspects of the research for the 2011-12 reporting period. Additional details about sub-tasks are provided in subsequent sections.

### I. SUMMARY OF WORK

***A grand challenge in cardiology since early 1950s is the development of an artificial heart that can replace a failing heart.*** The overall objective of our project is to help improve the care of battlefield-related cardiac injuries by providing novel methods to design and fabricate 3-D models of cardiac sub-components critical in restoring heart function.

We report the integration of dielectrophoresis (DEP) with stereolithography (SL) apparatus for the spatial patterning of cells on custom made gold micro-electrodes. We showed the patterning and encapsulation of mouse embryonic stem cells and skeletal muscle myoblasts. The mESCs showed high viability in both the DEP and the no DEP hydrogel samples, for a robust and flexible *in vitro* platform for stem cell differentiation and tissue engineering by mimicking elements of the native 3D *in vivo* cellular micro-environment.

A method was developed that controlled temporal and spatial degradation of a drug-encapsulating hydrogel. It was demonstrated that a sequential drug delivery can be attained with the hydrogel created in this study, and that the sequential delivery of two complementary proangiogenic factors can significantly increase vascular density in a target tissue.

To test hydrogel constructs *in vivo* we developed a mouse myocardial infarction model. We further characterized the model with echocardiography and histology staining. Stem cell populations were generated and characterized using bone marrow cells and adhesive formulations were tested on the heart surface for attaching patches to living muscle tissue.

We demonstrated a novel single-mode continuous-wave narrow bandwidth emission and widely tunable external cavity laser biosensor, representing a different approach to the problem of achieving high  $Q$ -factor resonance and simultaneously high-sensitivity for label-free resonant optical biosensors, for a broad array of applications in life science research, pharmaceutical screening, diagnostics, and environmental monitoring.

The progress detailed in the 2011-12 report has been made during the no-cost extension phase of the project.

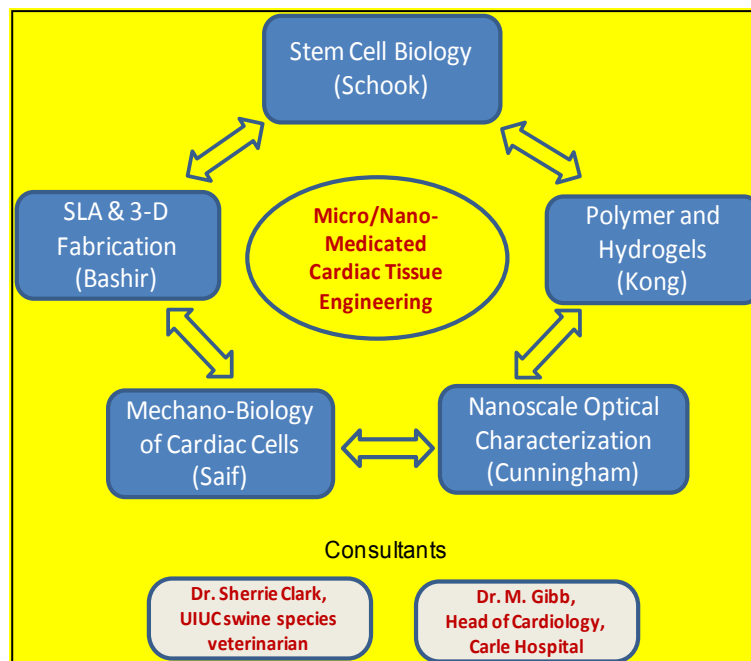
### II. INTRODUCTION

The regeneration of cells and tissue after injury or trauma is critical to medical and civilian communities. Cardiac injuries and regenerative engineering poses specific challenges since cardiac myocytes, the primary cells responsible for the mechanical beating of the heart muscle, do not regenerate. The cardiac system poses a significantly challenging problem in tissue

engineering due to the complex 3-dimensional mechano-actuation properties of the cardiac cells. ***A grand challenge in cardiology since early 50s is the development of an artificial heart that can replace a failing heart.*** Until today, artificial heart is used only for the temporary use (hrs) until a healthy donor heart is found. The latter is difficult to get, and is often rejected by the body after successful replacement. This very limited success in heart replacement, in spite of considerable effort and resources invested so far, calls for a new paradigm in the approach to heart replacement. This project attempts to offer such a paradigm by proposing to "grow" the heart or its components from the basic building blocks, namely the cells (differentiated cardiomyocytes) of the patient, biomaterials design, namely the hydrogel scaffolds to house the cells, and nanotechnology, namely the stereo-lithographically-patterned 3D substrate. New knowledge on cells' response to mechanical cues, and recent findings on cardiomyocyte functionality on mechanically tuned substrates from our labs form the basis for the project. In summary, stem cell differentiation in scaffolds, novel 3-D fabrication technologies, use of the appropriate biomaterials, integration of peptides for cardiac cell attachment and cell growth, the characterization of the scaffold materials and the transmembrane proteins, and cardiac cell mechanics are all critical elements of a comprehensive design approach proposed in this project for 3-D cardiac tissue engineering.

This project offers the use of 3-D stereolithography for fabricating the hydrogel scaffolds with cardiac cells, and nanoscale mechanical and optical tools for characterization of cardiac cells and their interactions with the scaffolds. ***Our objectives are to integrate these multi-disciplinary efforts and develop the strategies and methodologies for novel designs of 3-D components of an artificial heart.***

The project overview and research thrusts for each of the co-PIs are provided in the figure below, and the following table enlists third year project goals:





<b>Year 3 Project Goals continued (no-cost extension phase of the project)</b>	
1	Interface DFB laser biosensor and detection instruments w/ engineered cell scaffolds and observe cell membrane activity during cell seeding, proliferation, exposure to pulsating flow, exposure to chemical compounds/ growth media.
2	To demonstrate and characterize the capability of using SL to design and generate complex 3-D tissue with tunable architecture
3	Measure cardiac myocyte beating frequency versus material stiffness.
4	Develop 2D cantilever substrates with cardiac cells to explore the range of deformation and the frequencies of the cantilevers.
5	Demonstrate improved cardiac tissue function in hydrogels with properties optimized via <i>in vitro</i> cell studies.

### III. BODY

Potential Military Relevance. Battlefield trauma resulting in a variety of injuries is of significant concern to our military and civilian administration. Tissue engineering or regenerative medicine offers viable alternatives to counter many such injuries. ***Our project envisages improving the care of battlefield-related cardiac injuries by providing novel methods to design and fabricate 3-D models of cardiac sub-components that would be critical in restoring the function of the heart.*** According to the report on 'Capturing the power of biomaterials for military medicine'(NRC Report,2004), four areas in which enhancement of biomaterials and biotechnology will have a major impact on acute, chronic, and rehabilitation care in military medicine are (1) wound care, (2) tissue engineering, (3) drug delivery, and (4) physiological sensors and diagnostics. Our target area of research in cardiac tissue engineering, addresses one of the critical needs for the care in military medicine. The ultimate goals of our research are to resolve chronic medical problems and ultimate rehabilitation of injured military personnel (NRC Report, 2004). Our approach of using a mobilized cell population also provides flexibility in obtaining human MSCs in the field. They could be harvested from the soldiers and banked so they would have a source of their own cells. This approach is much faster and safer than bone marrow derived cells. The scaffolds we will develop could also be loaded with drugs that would be released over time to allow minimizing rejection by the body. Clearly, new methods for development of engineered tissues will have many applications beyond cardiac tissue engineering to engineering of vessels, skin, and many other organs.

### IV. KEY RESEARCH ACCOMPLISHMENTS

- A robust and flexible *in vitro* platform was developed to enable various applications in stem cell differentiation and tissue engineering by mimicking elements of the native 3D *in vivo* cellular micro-environment.
- Hydrogels modified with collagen greatly increased adhesion. The new formulation of Glutaraldehyde-BSA (GBSA) glue was used to adhere collagen modified patches to the thigh muscle of mouse cadavers. Patches firmly adhered to the muscle tissue. The adhesive

without patch was next tested on living cardiac tissue. GBSA was tested for toxicity in the mouse thoracotomy model. GBSA was placed on the heart surface and mice were revived and monitored.

- A method was developed to control temporal and spatial degradation of a drug-encapsulating hydrogel. It was demonstrated that the sequential delivery of two complementary proangiogenic factors significantly increased vascular density in a target tissue.
- Our work demonstrated several new capabilities of photonic crystal biosensors using photonic crystal enhanced microscopy (PCEM), enabling visualizing of dynamic cell attachment at much higher resolution and sensitivity for highly detailed quantification of attachment distribution within individual cells. This provides us a novel tool for the study of cell attachment in many contexts, including wound healing, cell culture optimization, stem cell differentiation, and cancer metastasis.

## V. REPORTABLE OUTCOMES

### List of Publications Accepted/Published in Peer-Reviewed Journals

- [1] P. Bajaj, D. Marchwiany, C. Duarte, R. Bashir, *Advanced Healthcare Materials* **2012** (accepted).

#### List of papers published in peer-reviewed Journals

1. Jeong, J., Cha, C., Chan, V., Zorulutuna, P., Bashir, R., & Kong, H.J. Stereolithographic assembly of proangiogenic microvascular stamp. *Advanced Materials* 24: 58-63 (2012). – Cover article, highlighted by C&EN & Chemical Engineering Progress.
2. Chan, V., Collens, M.B., Jeong, J.H., Kong, H.J. & Bashir, R. Directed cell growth and alignment on protein-patterned 3D hydrogels with stereolithography. *Virtual and Physical Prototyping* (accepted, 2012).
3. Chan, V., Jeong, J., Kong, H.J., & Bashir, R. Multi-Material bio-fabrication of hydrogel cantilevers and actuators with stereolithography. *Lab on a Chip* 12:88-98 (2012).
4. 1.EA, Lidstone, V. Chaudhery, A, Kohl, V Chan, T Wolf-Jensen, R Bashir, B.T. Cunningham. “Label-Free Imaging of Cell Attachment with Photonic Crystal Enhanced Microscopy”, *Analyst*, 2011, 136 (18), 3608 - 3615
5. C. Ge, M. Lu, Yafang, Tan and B. T. Cunningham, "Enhancement of pump efficiency of a visible wavelength organic distributed feedback laser by resonant optical pumping", *Optics Express*, Vol. 19, Issue 6, p. 5086-5092, 2011.
6. Y.F. Tan, C.Ge, A. Chu, M. Lu, W. Goldshlag, J. Huang, A. Pokriyal, S. George,B.T. Cunningham, “Plastic-Based Distributed Feedback Laser Biosensors in Microplate Format”, *IEEE Sensors*, Vol. 12, Issue 5, p. 1174-1180, 2012.

7. C. Ge, M. Lu, S. George, C. Wagner, J. Zheng, A. pokhriyal J. G. Eden and B. T. Cunningham, "External cavity laser biosensor", Nature Communications, under review, May 2012 .
8. J. Zheng, C.Ge, C.J. Wagner, M. Lu, B.T. Cunningham, J.D. Hewitt, and J.G. Eden, "Tunable Ring Laser With Internal Injection Seeding and an Optically-Driven Photonic Crystal Reflector", Optics Express, Vol. 20, Issue 13, p. 14292-14301 (2012) (# authors contributed to this work equally)
9. Y.F. Tan, C.Ge, A. Chu, M. Lu, W. Goldschlag, J. Huang, A. Pokriyal, S. George, B.T. Cunningham, "Distributed Feedback Laser Biosensor Noise Reduction", IEEE Sensors, Vol. 12, Issue 5, p. 1174-1180, 2012.

#### List of abstracts and presentations in related conferences

1. J. Jeong, V. Chan, C. Cha, P. Zorlutuna, C. Sukotjo, R. Bashir, & H.J. Kong, Independent control stiffness and permeability of a cell-encapsulating hydrogel for tissue engineering, AIChE Meeting, Minneapolis, October 2011.
2. J. Jeong, V. Chan, C. Cha, P. Zorlutuna, C. Sukotjo, R. Bashir, & H.J. Kong, Patterning of functional neovessels using a 'living' microvascular stamp, Outstanding research award presentation at Illinois Workshop on RBTE Symposium, November 2011.
3. J. Jeong, V. Chan, C. Cha, P. Zorlutuna, C. Sukotjo, R. Bashir, & H.J. Kong, Independent control stiffness and permeability of a cell-encapsulating hydrogel for tissue engineering, BMES meeting, Hartford, October 2011.
4. Molly Melhem, Tor Jensen, Jae Hyun Jeong, Vincent Chan, Rashid Bashir, Hyunjoon Kong, Lawrence Schook. A Cardiac Patch for Delivering Therapeutic Stem Cells to the Heart Following Myocardial Infarction. EBICS Annual Retreat, Atlanta, GA. June, 2011.

## **VI. CONCLUSION**

The mouse infarction model generated and characterized by us will be a flexible platform to test the application of stem cell deliver methods to infarcted cardiac tissue. The adhesives and stem cell populations tested and characterized will be used to measure improvement in cardiac function with and without stem cell application. These materials will also have utility for the targeted, prolonged delivery of stem cells or slow release drugs in other soft tissue applications.

The novel, implantable proangiogenic hydrogel patch developed in the project can potentially improve quality of revascularization therapies.

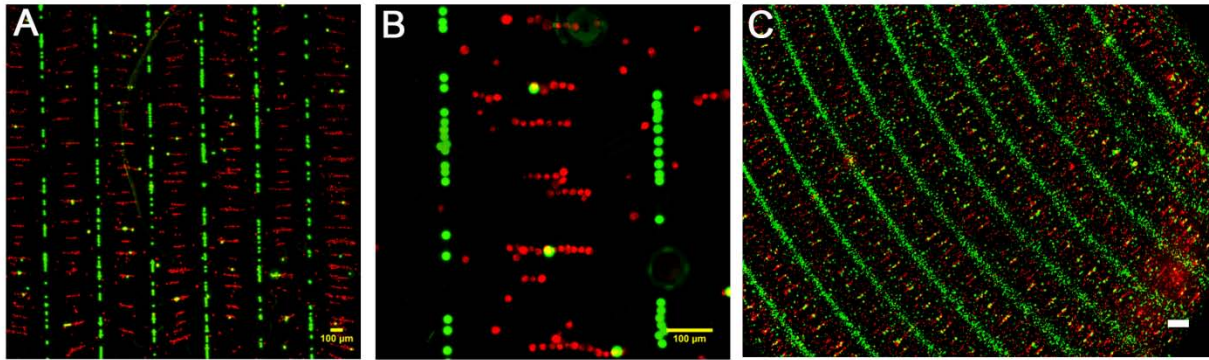
## SECTION II: Annual Report from Project Subgroups

### Research Group: Rashid Bashir

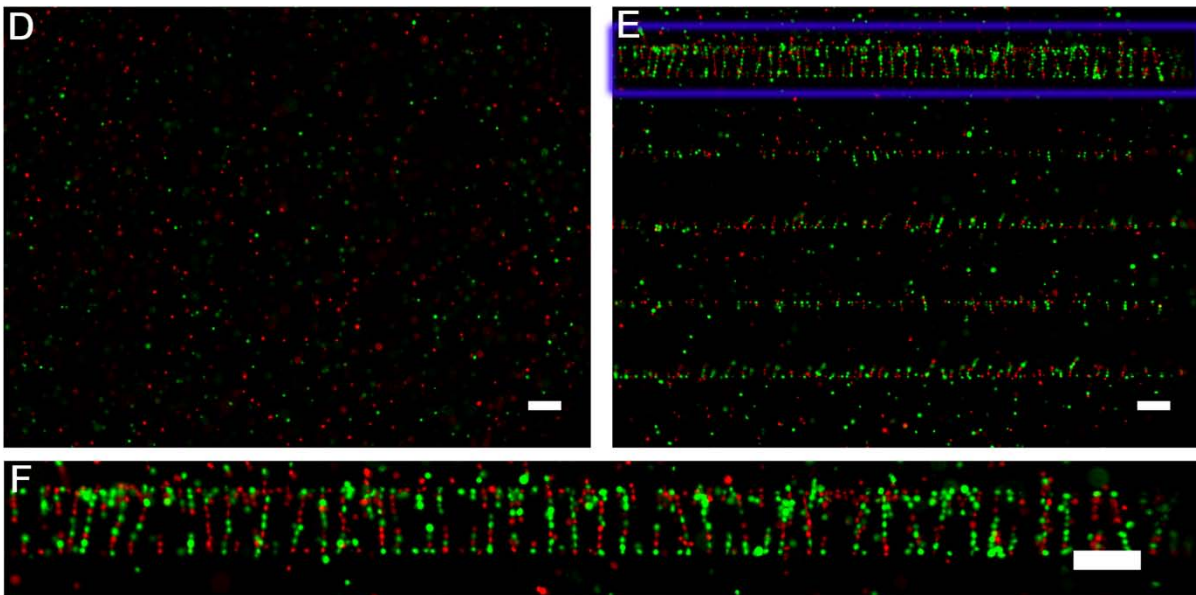
Period Sept'11 to Sept'12

Controlling the assembly of cells in three dimensions is very important for engineering functional tissues, drug screening, probing cell-cell/cell-matrix interactions, and studying the emergent behavior of cellular systems. Although the current methods of cell encapsulation in hydrogels can distribute them in three dimensions, these methods typically lack spatial control of multi-cellular organization and do not allow for the possibility of cell-cell contacts as seen for the native tissue. Here, we report the integration of dielectrophoresis (DEP) with stereolithography (SL) apparatus for the spatial patterning of cells on custom made gold micro-electrodes. Afterwards, they are encapsulated in polyethylene (glycol) diacrylate (PEGDA) hydrogels of different stiffnesses. This technique can mimic the *in vivo* microscale tissue architecture, where the cells have a high degree of three dimensional (3D) spatial control. As a proof of concept, we show the patterning and encapsulation of mouse embryonic stem cells (mESCs) and C2C12 skeletal muscle myoblasts. mESCs show high viability in both the DEP ( $91.79 \pm 1.4$  %) and the no DEP ( $94.27 \pm 0.5$  %) hydrogel samples. This robust and flexible *in vitro* platform can enable various applications in stem cell differentiation and tissue engineering by mimicking elements of the native 3D *in vivo* cellular micro-environment.

### Controlled patterning of particles over large areas



### Multi-cell interaction



### High viability

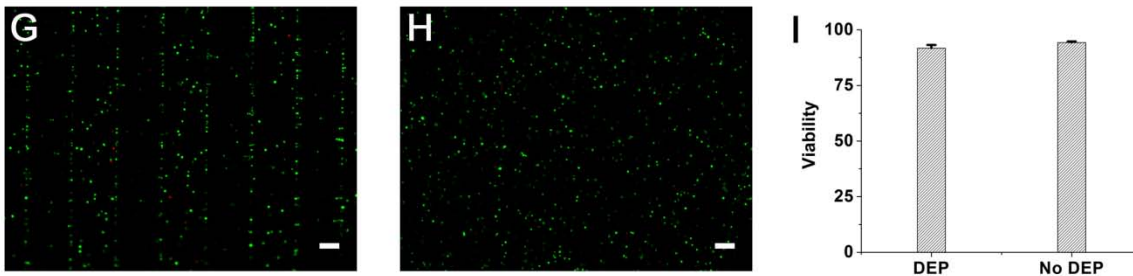


**Figure 1:** Multi-cell patterning and encapsulation in different stiffness hydrogels by using DEP and SL apparatus (A-C) This platform can be used to create large scale patterns of mammalian cells in 3D hydrogels. (A) C2C12 (red) cells (pDEP) and PS beads (green) (nDEP) in 15% PEGDA 700 (Scale bar = 100 µm) (B) Zoomed image of (A) (Scale bar = 100 µm) (C) mESCs

(pDEP) and PS beads (green) (nDEP) in 20% PEGDA 700 (Scale bar = 200  $\mu\text{m}$ ) by using spiral electrodes. (D-F) mESCs with two different colored dyes (red and green) were encapsulated in 15% PEGDA 3400. (D) Without DEP (Scale bar = 100  $\mu\text{m}$ ). (E) With DEP (Scale bar = 100  $\mu\text{m}$ ). (F) Zoomed image of the highlighted blue box clearly showing cell-cell interactions in the hydrogel (Scale bar = 100  $\mu\text{m}$ ). (G-I) Demonstrates that high cell viability can be achieved using this platform. (G) Live/dead assay at day 0 with DEP (Scale bar = 100  $\mu\text{m}$ ). (H) Live/dead assay at day 0 without DEP (Scale bar = 100  $\mu\text{m}$ ). (I) Graph showing the viability of cells with and without DEP. Green indicates live cells and red shows dead cells ( $n = 5$ ). Viability was calculated by counting the red cells, green cells and taking the ratio of green cells to the total number (green + red) of cells.

Figures 1D-F shows the encapsulation of mESCs with two different colored dyes (green and red) in 15% PEGDA 3400. By encapsulation of multiple types of cells using conventional SL, the two different types of cells are generally present with minimal cell-cell contacts in the hydrogel (Figure 1D). While these co-culture studies can be very useful for studying paracrine signaling<sup>[2]</sup>, cell-cell contacts which are responsible for fate decisions by embryonic stem cells cannot be studied using this approach.<sup>[3]</sup> However, as seen in figures 1E and F, DEP allows cell-cell contacts by formation of cellular pearl chains. These pearl chains can be used for studying the fate decisions by stem cells. Numerous studies have demonstrated the role of cellular co-culture for determining the fate of ESCs.<sup>[4, 5]</sup> This combined DEP-SL apparatus platform will enable the study of multiple cell interactions via cell-cell contacts in 3D and can open new doors in stem cell biology.

Figure 1G, H shows the image of a live/dead assay for mESCs with and without DEP on day 0 in 15% PEGDA 3400. It can be seen from these fluorescent images that most of the cells survive patterning via DEP and SLA encapsulation. Figure 1I quantifies the viability of cells with and without DEP. The cells which were aligned in the hydrogel with DEP show a viability of  $91.79 \pm 1.4\%$  while those which were not subjected to DEP show a slightly higher viability of  $94.27 \pm 0.5\%$ . Thus these studies show that our combined platform can be used for studying multi-cell interactions in 3D hydrogels while maintaining their viability.

## References:

- [1]W. Lee, N.-J. Cho, A. Xiong, J. S. Glenn, C. W. Frank, *Proceedings of the National Academy of Sciences* **2010**, 107, 20709.
- [2]J. H. J. Pinar Zorlutuna, Hyunjoon Kong, and Rashid Bashir, *Advanced Functional Materials* **2011**, 21, 3642
- [3]F. Soncin, L. Mohamet, D. Eckardt, S. Ritson, A. M. Eastham, N. Bobola, A. Russell, S. Davies, R. Kemler, C. L. R. Merry, C. M. Ward, *Stem Cells* **2009**, 27, 2069.

[4]R. Passier, D. W.-v. Oostwaard, J. Snapper, J. Kloots, R. J. Hassink, E. Kuijk, B. Roelen, A. B. de la Riviere, C. Mummery, *Stem Cells* **2005**, 23, 772.

[5]A. Soto-Gutierrez, N. Navarro-Alvarez, D. Zhao, J. D. Rivas-Carrillo, J. Lebkowski, N. Tanaka, I. J. Fox, N. Kobayashi, *Nat. Protocols* **2007**, 2, 347.

### **Resulting publications:**

[1] P. Bajaj, D. Marchwiany, C. Duarte, R. Bashir, *Advanced Healthcare Materials* **2012** (accepted).

## **Research Group: Taher Saif**

Period Sept'11 to Sept. 2012

### **Cardiomyocyte synchronization on thin PDMS films**

#### **I. SUMMARY OF WORK**

The synchronous contraction of many cardiomyocytes is critical for proper function of the heart. The development of synchronicity is an incompletely understood event of biological significance with known mechanical, electrical, and chemical factors. We present the use of a thin suspended PDMS membrane as a characterizable environment to study the emergence of synchronized contractions of primary cardiomyocytes.

A 10 micron thick PDMS film is suspended, taut, on a circular glass ring. The membrane is functionalized with Fibronectin. Primary cardiomyocytes extracted from 3 to 5 day old neonatal rats are seeded on the membrane and cultured in DMEM with 10% FBS. Initially, individual cardiomyocytes beat periodically, but with non-uniform phase and frequency. After 3-4 days, the contraction rhythm of the culture synchronizes with constant period. The simultaneous contraction of many cardiomyocytes is sufficient to deform the entire membrane in plane, with an amplitude of approximately 5  $\mu\text{m}$ . By freeing a 4 mm diameter section of the film, the net contractile force is sufficient to propel the film through the suspending media by swimming.

To quantify the development of the synchronization, particle tracking software is used to identify contractile cells throughout a single 2 mm diameter field of view. A set of waveforms  $f^i(t)$  is generated for each identified contracting cell  $i$ . A discrete set of events identifying the time of each individual contraction  $j$  of cell  $i$  (denoted  $t_j^i$ ) is measured. With no external stimulation, a reference waveform must be chosen to measure the degree of synchronization. The reference



waveform is chosen to be the measured contractile waveform that minimizes the distribution of time lags between each peak in the reference and the corresponding peaks in all other cells. In particular,  $f^{ref}(t)$  is chosen as the  $f^k(t)$  that minimizes  $\sum_{i,j} |t_j^k - t_j^i|$ . The width of the distribution of the set of peak offsets is expected to collapse as a culture synchronizes. Figure *b* illustrates the evolution of this distribution for a sample on days 2, 3, and 4 (left to right) after initiating the culture.

Further work will be directed at modifying the configuration of the PDMS membrane to individually probe the significance of mechanical and chemical factors in the synchronization of cardiomyocytes. By culturing cardiomyocytes on both sides of a single membrane, and isolating the chemical environment of each side, individual cultures will only be able to communicate by stretching the substrate. Successful synchronization in this system will demonstrate that mechanical communication is sufficient for cardiomyocyte synchronization. By adding stiff regions to the membrane, where stretching of the substrate will be trivially small, we can evaluate the ability of a culture on either side of the stiff region to synchronize to each other by chemical and electrical means. Such investigations may prove to be physiologically relevant, as many forms of heart disease involve stiff scar tissue in the heart.

## **Research Group: Larry Schook**

**Period Sept '11 to Sept '12**

### **Deliverables addressed:**

Year 3 cont'd.

- To demonstrate and characterize the capability of using SL to design and generate complex 3-D tissue with tunable architecture.
- Demonstrate improved cardiac tissue function in hydrogels with properties optimized via in vitro cell studies.

## **I. Summary of Work**

In order to test hydrogel constructs *in vivo* we have developed a mouse myocardial infarction model. We have further characterized the model with echocardiography and histology staining. Stem cell populations were generated and characterized using bone marrow cells and adhesive formulations were tested on the heart surface for attaching patches to living muscle tissue.

## **II. Introduction**

The goals for the Schook group were to develop an *in vivo* model capable of testing practical applications for hydrogel heart patches. The mouse model was chosen for initial testing due to its relative simplicity and widespread use in testing new cardiac materials and methods.



### III. Body

**Echocardiogram testing:** To obtain a measure of heart function before and after experimental infarction we used echocardiography. Animals are measured 24 hours prior to procedure to obtain baseline measurements and again 7 days after the procedure to evaluate extent of damage due to experimental infarct. Figure one A and B shows a typical response with ejection fraction decreasing from 65% to 21% and diastolic volume increasing from 68 uL to 122 uL. These measurements will be combined with histological measurements to evaluate overall tissue damage (or prevention of damage) during patch testing.

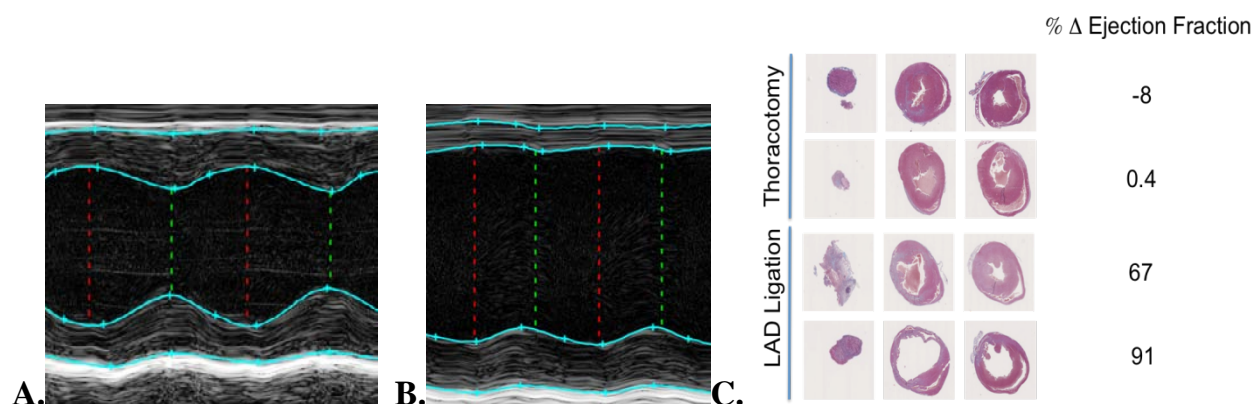


**Figure 1.** (A) Echocardiogram of healthy heart 24 hours prior to experimental infarction. (B) Echocardiogram of the same animal one week following experimental infarction. Images show ventricular enlargement, heart wall thinning, and decreased ejection fraction following infarct procedure. (C) Massons Trichrome staining results 1 week post-surgery. Red (muscle, cytoplasm, fibrin), Blue (collagen), Yellow (erythrocytes). Percent change in ejection fraction (EF) calculated as the change in EF 1 week post-surgery as a fraction of the measured EF prior to surgery.

**Histology staining:** Histological results were obtained at 1wk post-surgery from both control thoracotomy only and infarcted mice (figure 1C). In addition to wall thinning of the left ventricle, collagen deposition can be seen, indicating muscle depletion and scar tissue formation downstream of the ligated LAD. The reconstruction of the heart tissue is accompanied by a decrease in ejection fraction, as was calculated from echocardiogram ultrasound measurements.

**Adhesive testing:** The use of Glutaraldehyde-BSA (GBSA) glue was evaluated for adhering patches to the heart surface. Concentrations of BSA were tested based on the analysis of Berchane et al. (J Mater Sci: Mater Med (2008) 19: 1831-1838). A concentration of BSA at 15 wt/vol% with a glutaraldehyde concentration of 1.33% provided a functional gelation time (approximately 60-90 seconds). Initial testing showed poor adhesion to unmodified hydrogels. Hydrogels modified with collagen greatly increased adhesion. The new formulation of GBSA

glue was used to adhere collagen modified patches to the thigh muscle of mouse cadavers (Figure 2). Patches firmly adhered to the muscle tissue. The adhesive without patch was next tested on living cardiac tissue. GBSA was tested for toxicity in the mouse thoracotomy model. GBSA was placed on the heart surface and mice were revived and monitored for one week. There were no deaths in the GBSA animals and no differences in animal activity compared to control thoracotomy. Histology of the heart sections is underway to determine if significant inflammatory invasion or remodeling of the heart wall occurred due to the presence of the glue.

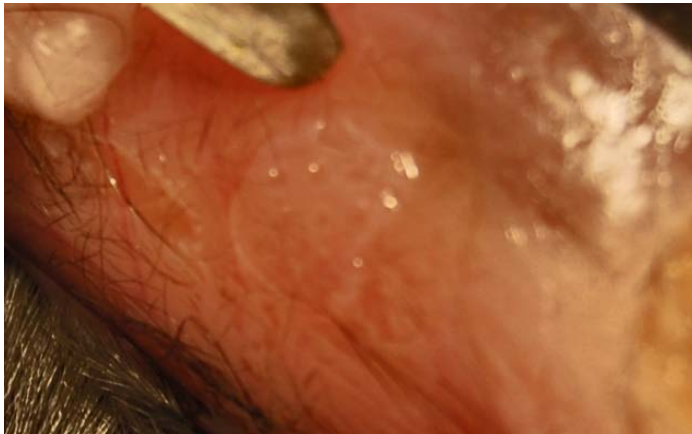


**Figure 2.** Patterned hydrogel patch adhered to mouse thigh muscle using a glutaraldehyde glue formulated to be similar to the commercial product BioGlue (CryoLife).

*Stem cell populations:* Mouse stem cells were isolated from the tibias and femurs of healthy C57BL/6 mice. The heterogeneity of enriched populations is tested via surface marker expression (Sca-1 expression as the primary stem cell marker; CD45 to differentiate mesenchymal from hematopoietic stem cells). Candidate transplantation cells were generated and characterized by flow cytometry. Mouse bone marrow cells were isolated from the long bones of 9 week old mice. MSC populations were enriched use plastic adherence techniques and the resulting population was characterized by flow cytometry. Target MSC populations are Sca1+/CD45- (Figure 3). Early passages show approximately 90% Sca1+ cells and 70% Sca1+/CD45- MSC population.

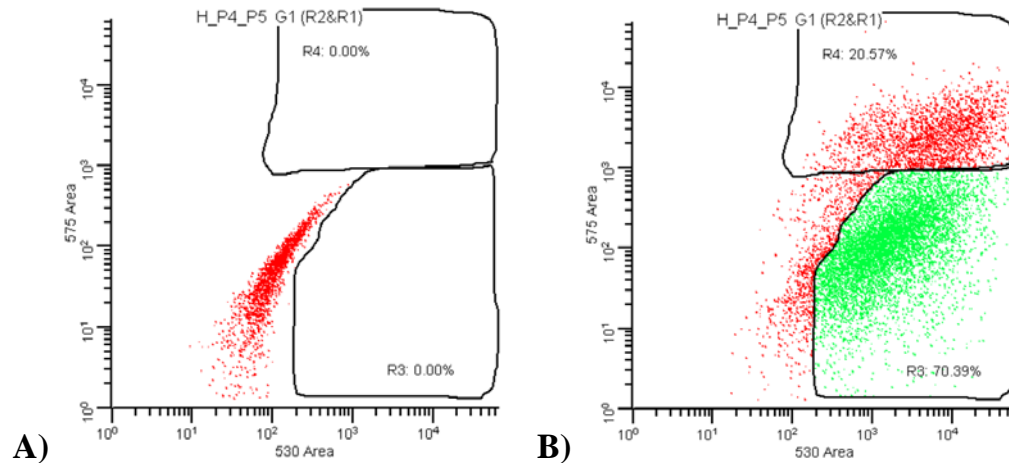


**Figure 3.** Flow cytometric analysis of mouse bone marrow MSC population. The markers for CD45 (575 Area) and Sca1 (530 Area) were used to characterize the population. Negative control staining (A) and dual antibody staining (B) are shown.

#### IV. Key Research Accomplishments

- Functional characterization of mouse myocardial infarction model
- Testing of GBSA adhesive formulation for use on cardiac tissue
- Production and characterization of stem cell population for transplantation

#### V. Reportable Outcomes

- Molly Melhem, Tor Jensen, Jae Hyun Jeong, Vincent Chan, Rashid Bashir, Hyunjoon Kong, Lawrence Schook. A Cardiac Patch for Delivering Therapeutic Stem Cells to the Heart Following Myocardial Infarction. EBICS annual retreat, Atlanta, GA. June, 2011.

#### VI. Conclusion

The mouse infarction model we have generated and characterized will be a flexible platform to test the application of stem cell deliver methods to infarcted cardiac tissue. The adhesives and stem cell populations tested and characterized will be used measure improvement in cardiac function with and without stem cell application. These materials will also have utility for the targeted, prolonged delivery of stem cells or slow release drugs in other soft tissue applications.

## **Research Group: Hyunjoon Kong**

Period Sept'11 to Sept'12

### **I. SUMMARY OF WORK**

**Kong's group's goal was to build a microvascular stamp using 3D stereo-lithographic technology to guide and pattern blood vessel formation.**

Aim 1: To adapt the 3D stereo-lithographic apparatus for biological components (*i.e.* living cells, photopolymerizable hydrogels, and signaling proteins)

Aim 2: To develop a novel photo-polymerizable hydrogel matrix that decouples elastic modulus and swelling ratio

Aim 3: To demonstrate blood vessel patterning using microvascular stamps implanted on chick chorioallantoic membranes (CAMs)

### **II. INTRODUCTION:**

Neovessels play a critical role in homeostasis, regeneration, and pathogenesis of tissues and organs, and their spatial organization is a major factor in influencing vascular function. Therefore, successful treatments of wounds, ischemic tissue, and tissue defects greatly rely on the ability to control the number, size, spacing, and maturity of blood vessels regenerated within a target tissue. However, technologies to control the spatial organization of mature neovessels in vivo over physiologically-relevant length scales are still lacking. Here, we present a hydrogel that can release dual proangiogenic growth factors in a sequential manner, and thus enhance the vascular regeneration in an implantation site.

In this work, a composite hydrogel comprising of two distinct domains, poly(ethylene glycol) dimethacrylate (PEGDMA) and polyethyleneimine (PEI) & PEGDA, was fabricated by initially generating PEGDMA microwells via soft lithography and then filling the microwells with the PEI & PEGDA hydrogel. Two different types of angiogenic growth factors, VEGF 165 and VEGF 121, were incorporated into these hydrogel domains where VEGF 165 was encapsulated in the poly(lactic acid-co-glycolide) (PLGA) particles and then dispersed in the PEGDMA hydrogel as VEGF 121 was directly loaded in the PEI & PEGDA filling in the PEGDMA microwells.

### **III. BODY:**

Encapsulation of drug in the PLGA particles that were trapped in the PEGDMA hydrogel provided the sustained drug release up to two weeks. Also a unique rapid degradation of the PEI & PEGDA hydrogel from predefined locations has launched the sequential and spatial drug

release. Dual drug loaded composite hydrogel was implanted onto the chick chorioallantoic membrane to examine the angiogenic response to the spatial, sequential, and sustained drug delivery.

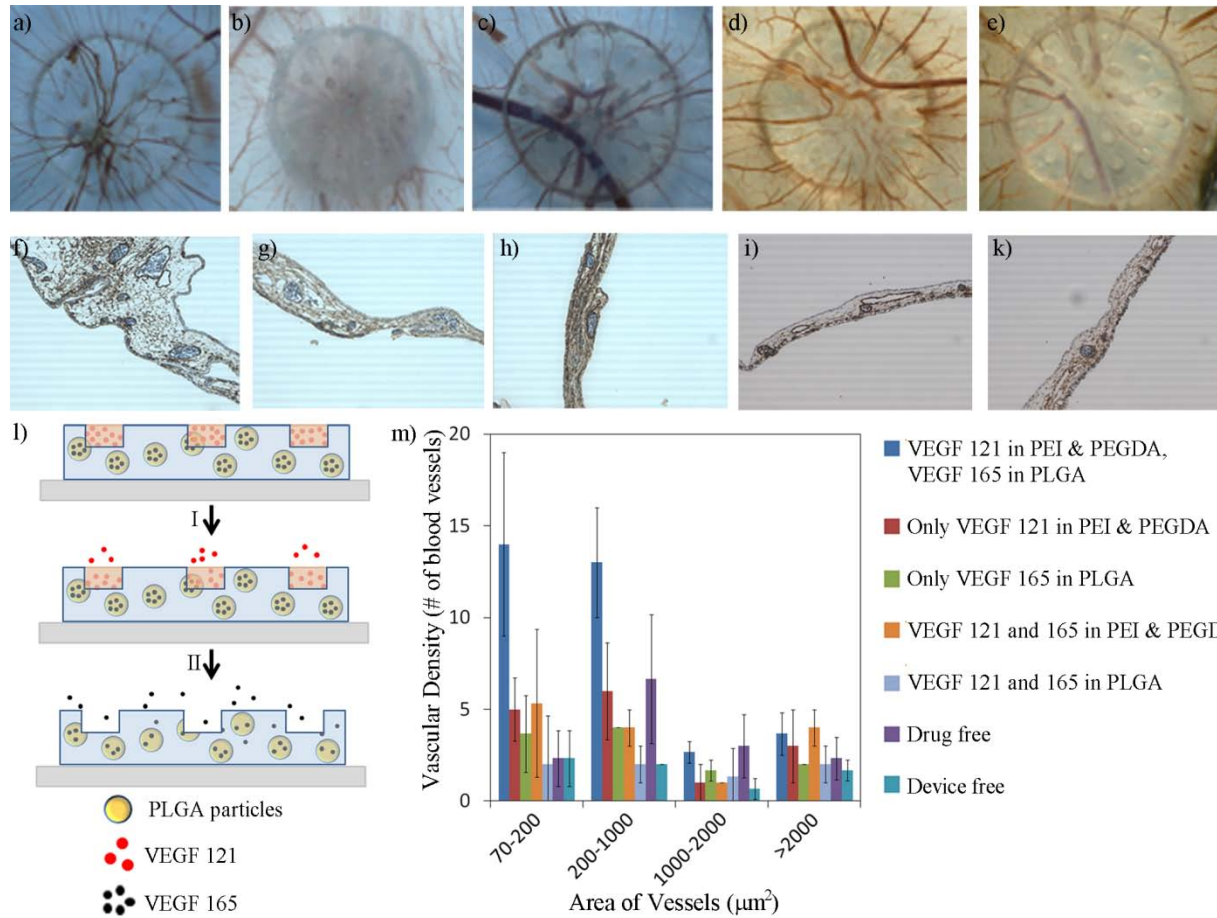


**Figure.** Neovessel formation on chick chorioallantoic membrane (CAM) (a- k). Optical images (a- e) and the histology images that are positively stained by an antibody to  $\alpha$ -smooth muscle actin ( $\alpha$ -SMA) (f- k) of the neovessels formation on the CAM in the presence of VEGF 121 in the PEI & PEGDA hydrogel and VEGF 165 in the PLGA particles (a and f), only VEGF 121 in the PEI & PEGDA hydrogel (b and g), only VEGF 165 in the PLGA particles (c and h), VEGF 121 and 165 in the PEI & PEGDA hydrogel (d and i), VEGF 121 and 165 in the PLGA particles (e and k). l) The mechanism of the sequential dual drug release from the composite hydrogel (cross-section). VEGF 165 (black) is encapsulated in the PLGA particles (yellow) which are embedded in the PEGDMA hydrogel (blue). VEGF 121 (red) is loaded in the PEI & PEGDA hydrogel (orange). VEGF 121 is first released from the composite hydrogel very fast as the PEI & PEGDA hydrogel degrades (I). Then, VEGF 165 is slowly released as it diffused out of the PLGA particles and the PEGDMA hydrogel (II). m) Quantification of the neovessel formation in the number of the blood vessels as a function of the vessel area.

#### IV. KEY RESEARCH ACCOMPLISHMENTS:

- Kong's group developed a method that can control temporal and spatial degradation of a drug-encapsulating hydrogel.
- Kong's group has demonstrated that a sequential drug delivery can be attained with the hydrogel created in this study.
- Kong's group has demonstrated that the sequential delivery of two complementary proangiogenic factors can significantly increase vascular density in a target tissue.

#### V. REPORTABLE OUTCOMES:

##### List of papers published in peer-reviewed Journals

1. Jeong, J., Cha, C., Chan, V., Zorlutuna, P., Bashir, R., & Kong, H.J. Stereolithographic assembly of proangiogenic microvascular stamp. *Advanced Materials* 24: 58-63 (2012). – Cover article, highlighted by C&EN & Chemical Engineering Progress.
2. Chan, V., Collens, M.B., Jeong, J.H., Kong, H.J. & Bashir, R. Directed cell growth and alignment on protein-patterned 3D hydrogels with stereolithography. *Virtual and Physical Prototyping* (accepted, 2012).
3. Chan, V., Jeong, J., Kong, H.J., & Bashir, R. Multi-Material bio-fabrication of hydrogel cantilevers and actuators with stereolithography. *Lab on a Chip* 12:88-98 (2012).

##### List of abstracts and presentations in related conferences

1. J. Jeong, V. Chan, C. Cha, P. Zorlutuna, C. Sukotjo, R. Bashir, & H.J. Kong, Independent control stiffness and permeability of a cell-encapsulating hydrogel for tissue engineering, AIChE Meeting, Minneapolis, October 2011.
2. J. Jeong, V. Chan, C. Cha, P. Zorlutuna, C. Sukotjo, R. Bashir, & H.J. Kong, Patterning of functional neovessels using a 'living' microvascular stamp, Outstanding research award presentation at Illinois Workshop on RBTE Symposium, November 2011.
3. J. Jeong, V. Chan, C. Cha, P. Zorlutuna, C. Sukotjo, R. Bashir, & H.J. Kong, Independent control stiffness and permeability of a cell-encapsulating hydrogel for tissue engineering, BMES meeting, Hartford, October 2011.

#### VI. CONCLUSION:

Overall, this study demonstrated a novel, implantable proangiogenic hydrogel patch that can potentially improve quality of revascularization therapies. In this unit, a sequential release of two complementary proangiogenic factors, VEGF121 and VEGF165, were critical to increase density of mature blood vessels at an implantation site.

## **Research Group: Brian Cunningham**

Period Sept'11 to Sept'12

**SECTION 1** LABEL-FREE IMAGING OF CELL ATTACHMENT WITH PHOTONIC CRYSTAL ENHANCED MICROSCOP.....

**SECTION 2** DISTRIBUTED-FEEDBACK LASER BIOSENSOR NOISE REDUCTION.....

**SECTION 3** EXTERNAL CAVITY LASER BIOSENSOR.....

**SECTION 4** PROGRESS REPORT ON PHOTONIC CRYSTAL ENHANCED MICROSCOPY.....

**APPENDIX**.....

## **Section 1**

### **Label-Free Imaging of Cell Attachment with Photonic Crystal Enhanced Microscopy**

#### ***Introduction***

This portion of the report documents improvements and progress with regard to the application of photonic crystal biosensors to characterize cell attachment density in response to various stimuli. Over the past three years, we have developed a new kind of microscope, capable of imaging cell attachment at the level of individual cells. After proving this capability in multiple contexts, we moved on to proving the utility of this technology in a biological context, uncovering several areas in need of improvement and optimization.

#### ***BODY***

### **Label-Free Imaging of Cell Attachment with Photonic Crystal Enhanced Microscopy**

#### **I. SUMMARY OF WORK**

We introduce photonic crystal enhanced microscopy (PCEM) as a label-free biosensor imaging technique capable of measuring cell surface attachment and attachment modulation. The approach uses a photonic crystal optical resonator surface incorporated into conventional microplate wells and a microscope-based detection instrument that measures shifts in the resonant coupling conditions caused by localized changes in dielectric permittivity at the cell-sensor interface. Four model systems are demonstrated for studying cancer cells, primary cardiac muscle cells, and stem cells. First, HepG2/C3 hepatic carcinoma cells were cultured and observed via PCEM in order to characterize cell adhesion in the context of growth and locomotion. Second, Panc-1 pancreatic cancer cells were used to verify that cell attachment density decreases in response to staurosporine, a drug that induces apoptosis. Third, we used PCEM to confirm the influence of integrin-mediated signaling on primary neonatal cardiomyocyte growth and development. Rounded cardiomyocytes consistently showed decreased cell attachment density as recorded via PCEM, while spreading cells exhibited greater attachment strength as well as increased contractility. Finally, PCEM was used to monitor the morphological changes and extracellular matrix remodeling of porcine adipose-derived stem cells subjected to a forced differentiation protocol. Each of these experiments yielded information regarding cell attachment density without the use of potentially cytotoxic labels, enabling study of the same cells for up to several days.



## II. INTRODUCTION

### **Goal of this investigation:**

Cell adhesion is a vital process for cell growth, proliferation, differentiation and motility, playing a central role in such varied phenomena as tissue growth and development, inflammation, wound healing, cancer metastasis, and myriad others [1-2]. For life science research and cell-based pharmaceutical screening applications, development of a more fundamental understanding of the factors influencing cell-substrate interactions requires the development of new tools. Current in vitro cell imaging techniques often rely either on cytotoxic stains or fluorescent labels to provide highly specific information; both of these techniques frequently permanently alter the state of the cell, and often require fixing or isolation of the samples to be considered for examination. Traditional light microscopy and phase contrast microscopy offer improvements in the lengths of possible experimentation, but at the expense of specific and relevant information regarding cell activity and metabolism. Here, we present photonic crystal enhanced microscopy (PCEM) as a label-free imaging biosensor technique for visualizing and quantifying complex cellular responses to multiple stimuli over prolonged periods of study.

### **How can PC biosensors act as a superior measurement tool?**

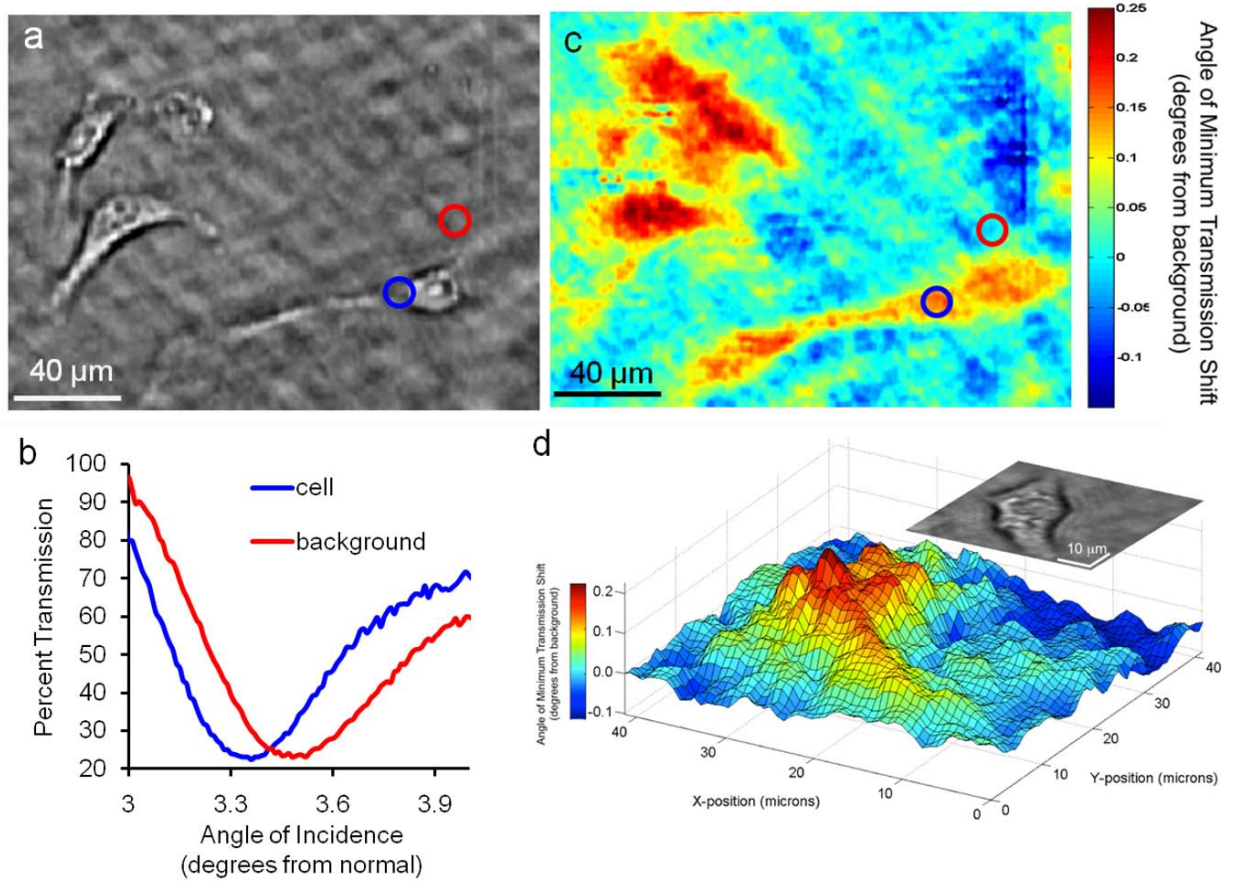
Photonic Crystal (PC) biosensors have been recently demonstrated as a high-resolution label-free detection technology that can be fabricated from plastic materials and incorporated into standard microplate formats for high throughput screening applications [3-4]. PC biosensors consist of a low refractive index sub-wavelength periodic grating structure that functions as a highly reflective optical resonator (see Fig. S1). While previously reported PC surfaces (also referred to as Guided Mode Resonant Filters) have been comprised of a rectangular grating profile with a period of 550 nm and a grating depth of approximately 150 nm, the biosensors used in this study have been modified to reduce possible effects of sensor morphology on the formation of cell attachments. To reduce the occurrence of such effects, the PC biosensors used in this study possess a period of 360 nm with a grating depth of approximately 30 nm. The addition of an intermediary SiO<sub>2</sub> layer allows for the exposed TiO<sub>2</sub> layer of the sensor to be deposited with a gradual curved profile in lieu of the rectangular profile used in previously documented sensors. Atomic force microscopy imaging was performed to verify surface morphology would have a minimal effect on cellular activity (see Supplementary Figure 1, online). It is worth noting that none of the cells investigated in this work exhibited polarization with respect to the grating structure. When illuminated by a collimated laser, the PC surface acts as a highly efficient light reflector only at a specific angle of incidence at which resonant coupling of incident light to the PC occurs (see Fig. S2). The resonant coupling angle is dependent upon the dielectric permittivity of material on the PC surface, and shifts to lower angles when cells or biomolecules become attached. Because the PC surface effectively prevents lateral propagation of resonantly coupled light, attachment of discrete objects, such as cells, results in a highly localized shift in the resonant coupling angle, thus opening up the potential for high resolution biosensor imaging. In this report, we present the use of a detection system based upon microscopy

that overcomes spatial resolution limitations of previously reported PC biosensor imaging systems [5-6] enabling, for the first time, label-free cell attachment images with 0.61  $\mu\text{m}^2$  pixel resolution. The detection system does not require physical contact to a coupling prism as required for imaging Surface Plasmon Resonance (SPR) [7-8], nor the a priori knowledge of the analyte necessary for ellipsometry [9-10], therefore enabling high throughput measurement of large numbers of cells within biosensor-embedded microplates, flow channels, and culture dishes.

### **What is the practical implementation of photonic crystal enhanced microscopy (PCEM)?**

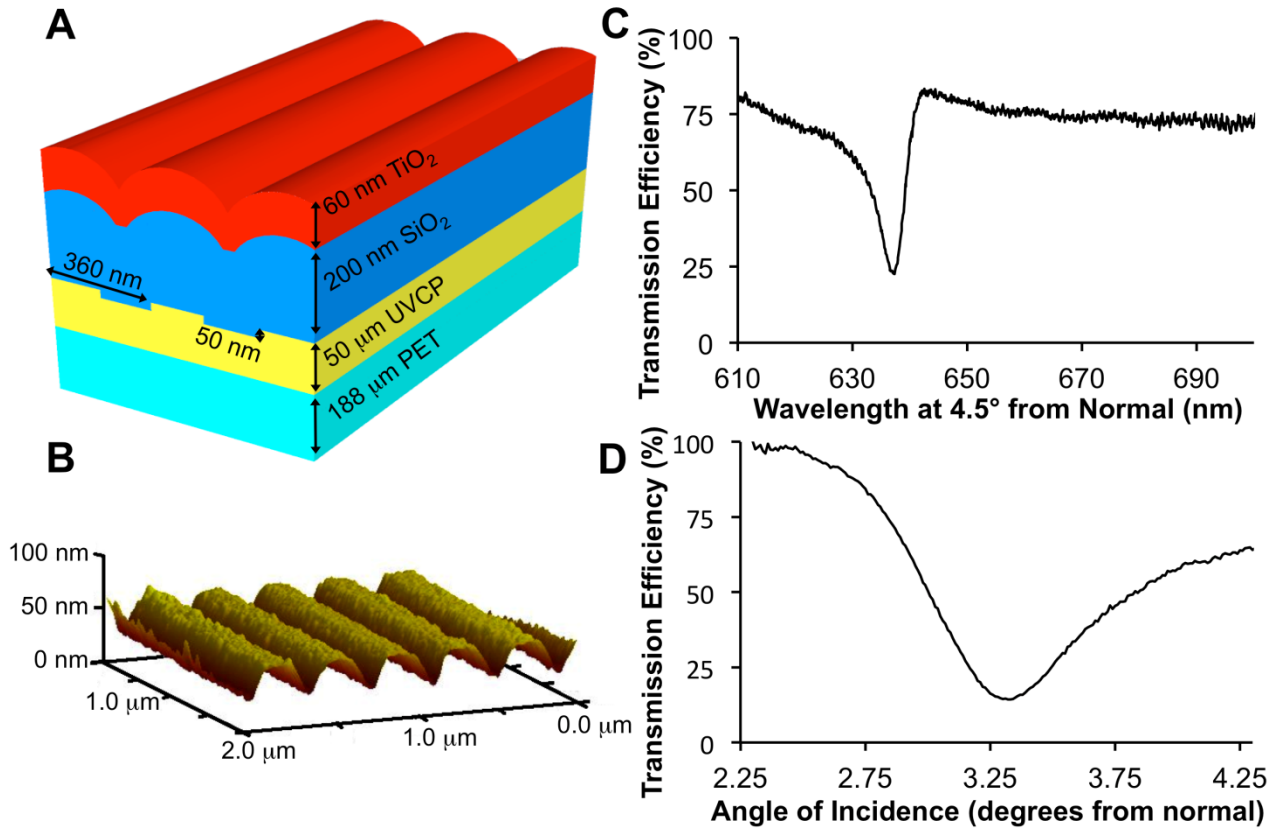
As shown in Figure S3, the PCEM instrument illuminates the PC surface from below with a collimated laser beam, which is rapidly scanned through a  $\sim 3^\circ$  range of incident angles at 0.01-degree increments with a computer-controlled rotating mirror. An image of transmitted light intensity is gathered through a 10x or 20x microscope objective onto a CCD camera for each incident angle (Figs. S3-S4). At the resonant coupling angle, the incident laser light is efficiently reflected, resulting in a minimum in transmitted intensity. Software determines the Angle of Minimum Transmission (AMT) on a pixel-by-pixel basis from the CCD images by fitting a second order polynomial function to the transmitted intensity versus angle curve (Fig. 1c). It is important to note that due to the limited penetration of the evanescent field region from the PC into the surrounding cell media (approx. 100 nm), PCEM is sensitive only to dynamic changes in biomaterial density at or near the cell surface, remaining unaffected by the presence and location of cellular organelles. As attachment, driven by the activity of integrins and filapodia, draws the cell into more intimate contact with the PC surface, there is a commensurate increase in the local dielectric permittivity that is clearly measurable (Fig. 1) [3]. Detection resolution is sufficient not only for observation of large angle shifts that differentiate cell from non-cell regions, but also for observation of subtle changes in attachment strength that result from motility, apoptosis, differentiation, and contraction.

Figure 1



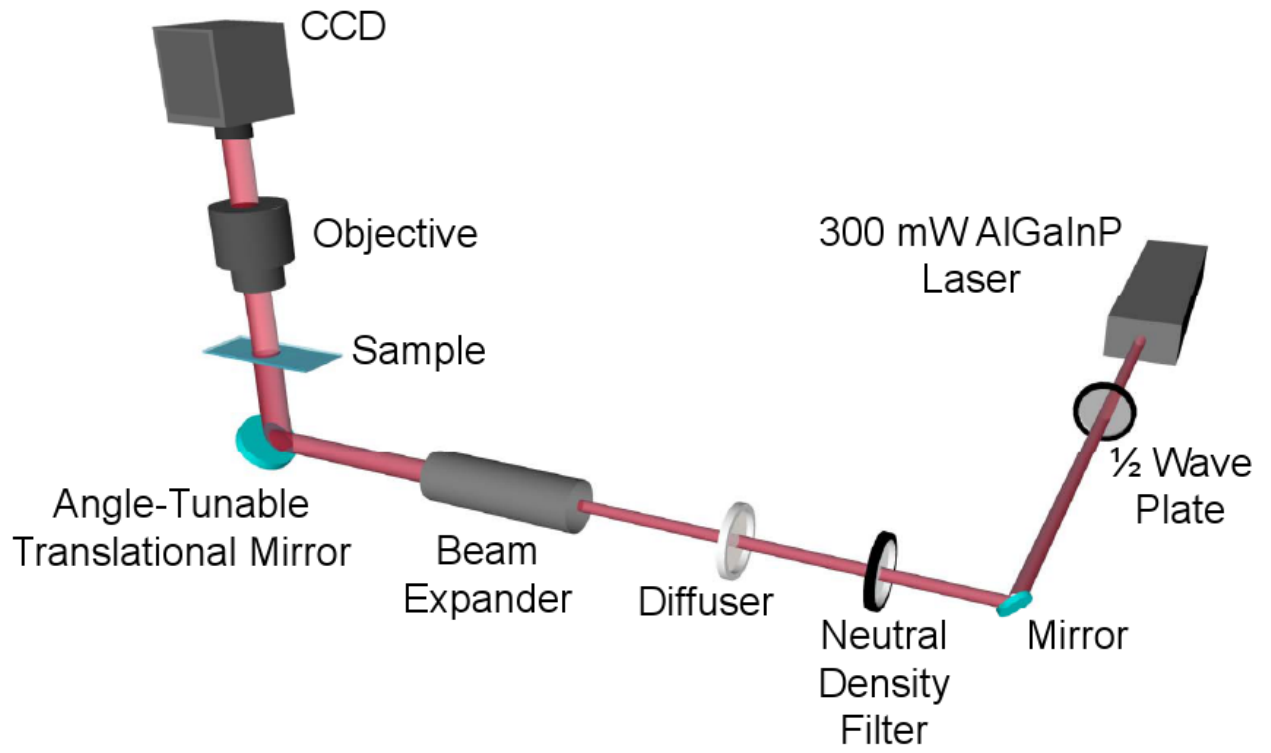
**Figure 1:** Summary of Photonic Crystal Enhanced Microscopy. a) Bright field microscopy of HepG2/C3 cells shows cell spreading and morphology. b) Transmission intensity is plotted as a function of angle of incidence for individual pixels on (blue) and off (red) a cell. Pixel regions are highlighted in (a). c) A composite PCEM image, describes the angle of minimum transmission (AMT) as a function of position. Attachment proteins deposited on the biosensor by viable cells result in a reduced angle of minimum transmission shift. d) A surface plot of cardiomyocyte attachment at 24h obtained via PCEM corresponds with the morphology observed in bright field microscopy (inset).

Figure S1



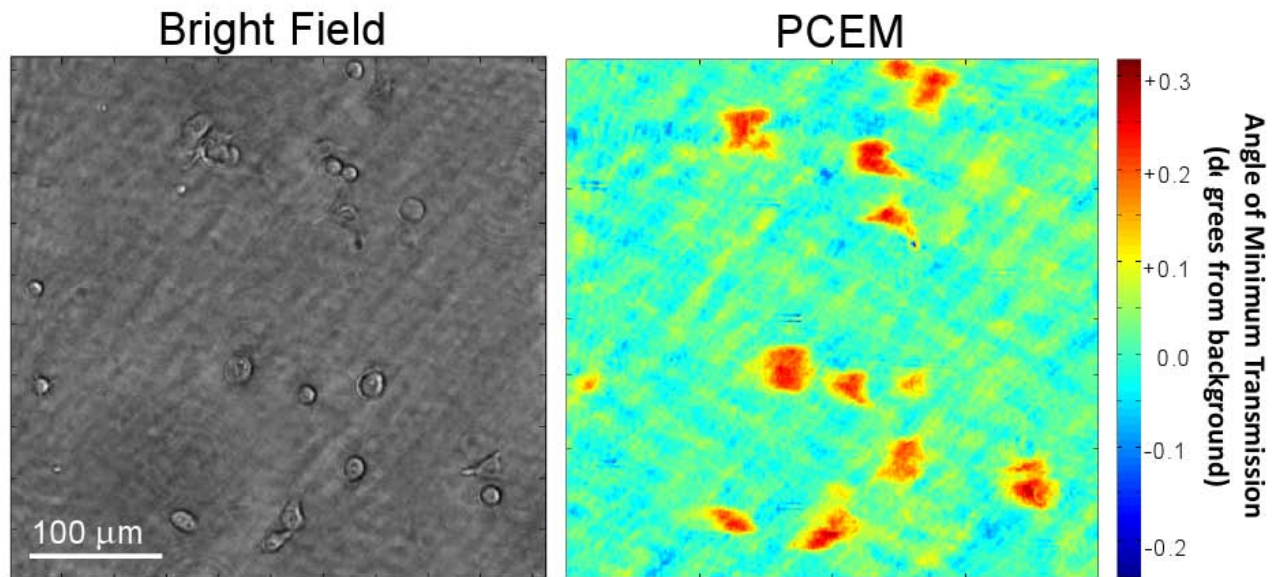
**Figure S1:** a) Schematic illustration of the PC biosensor configuration. A photoreplica molding process yields a grating pattern composed of UV-curable polymer (UVCP), which is affixed to a layer of polyethylene terephthalate (PET). The resulting grating is then coated with  $\text{SiO}_2$  and  $\text{TiO}_2$  to complete fabrication. b) Atomic force microscopy (AFM) image of a PC biosensor. c) PC biosensor characterization by wavelength. The resonant wavelength of a PC biosensor is rejected by the biosensor structure, resulting in decreased transmission efficiency. d) PC biosensor characterization by angle of incidence. The resonant angle of incidence in combination with the illumination using the resonant wavelength results in satisfaction of the resonant condition of the PC biosensor, resulting in decreased transmission efficiency.

Figure S2



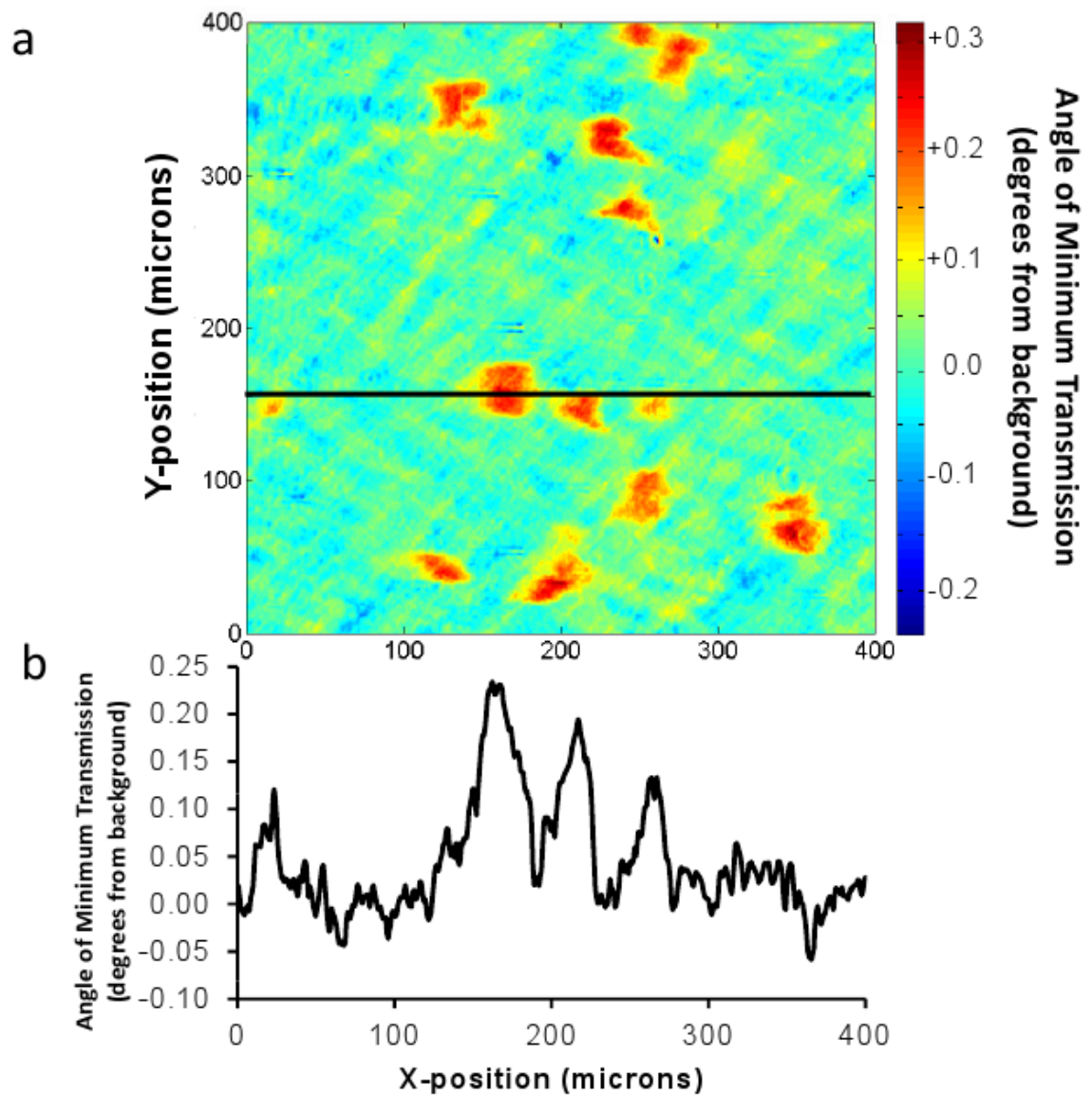
**Figure S2:** Schematic depiction of the photonic crystal enhanced microscope. Collimated 637 nm light emitted from a diode laser is directed into a  $\frac{1}{2}$  wave-plate for control of polarization before being attenuated by a variable neutral density filter. The beam is then directed through a diffuser and into a beam expander to provide a broadly uniform illumination source. The angle of incidence upon the sample is controlled by an angle-tunable mirror mounted on a translational stage. Transmitted light is magnified and focused by an objective lens and recorded by a CCD.

Figure S3



**Figure S3:** Wide-field capability of PCEM. PCEM imaging allows simultaneous label-free and bright field imaging of cell attachment over wide areas. At 20x magnification, the field of view encompasses an area of  $0.16 \text{ mm}^2$ .

Figure S4



**Figure S4:** PCEM Line Plot. HepG2/C3 hepatic carcinoma cells cultured for 2h show significantly increased attachment protein density, as indicated by PCEM (a) and a line plot taken across the AMT profiles of three cells (b).



### III. BODY

#### Methods

##### Instrument Description

The detection system used in our study is a modified back-illuminated fluorescent microscope (Olympus BX51WI) shown schematically in Fig. S3. The microscope is equipped with 10x and 20x objective lenses (N.A. = 0.25, 0.40, respectively) and an electron multiplying CCD (C9100-13 EM-CCD; Hammamatsu Inc.) for imaging. A 300-mW,  $\lambda=637$  nm AlGaInP diode laser is the excitation source. The laser light is passed through a rotating diffuser and then collimated by a beam expander. This sequence of optical components results in a spatially uniform, highly collimated beam that is then incident on a high-resolution motorized gimbal-mounted mirror, thus providing collimated illumination at a user-selectable incident angle. In order to maintain a constant illumination area on the device, the gimbal-mounted mirror sits on top of a motorized linear stage that translates laterally as the mirror rotates. As the collimated light at a fixed wavelength is incident on the PC surface, the angle of incidence can be tuned to allow the laser to couple with the PC resonance, thereby allowing maximum field coupling into the transverse electric (TE) mode of the PC. The excitation illumination was TE polarized by passing the laser light through a half-wave plate.

##### Device Fabrication

Fabrication of the device was performed using a plastic-based nanoreplica molding process [3]. Briefly, a silicon wafer with a negative surface volume image of the desired grating pattern was fabricated using deep-UV lithography and reactive ion etching. A liquid that contains an uncured monomer and a UV-activated polymerization initiator is sandwiched between a flexible plastic sheet and the silicon master wafer to enable the liquid to fill the silicon surface structure subsequent to curing with a high intensity UV lamp (Xenon, Inc). The hardened polymer grating preferentially adheres to the plastic substrate, and thus can be easily peeled away from the silicon. After the molding step, the replica was cut and attached to a  $1 \times 3$  in<sup>2</sup> microscope slide. An evaporated SiO<sub>2</sub> intermediate layer, ( $t_{\text{SiO}_2}$ )= 200 nm, (e-beam evaporation, Denton Inc.) was deposited on the grating surface to control the resonant peak width. After the SiO<sub>2</sub> deposition, ~60 nm of TiO<sub>2</sub> was deposited by RF sputtering (PVD 75, Kurt Lesker) using an *in-situ* process monitor to accurately achieve a resonance condition that nominally results in  $\lambda=637$  nm wavelength resonantly coupling to the PC surface at an incident angle of 4° in an aqueous environment. The device is bonded to a six well bottomless microplate using a transparent UV-curable adhesive (AC R260-A1, Addison Clear Wave). The plates were thoroughly rinsed and the wells were incubated with 70% ethanol for 15 min.

For Panc-1 and HepG2/C3 cell culture, the PC biosensors were coated with poly-*D*-lysine (MW = 70,000-150,000 Da, Sigma-Aldrich P6407) immediately prior to plating cells. For this purpose the wells were incubated with a 100 ng/ml solution in cell grade



phosphate buffered saline (PBS), pH = 7.4 for 15 min. After incubation, the wells were rinsed twice with PBS before cell media was added. For cardiomyocyte culture, bare sensor wells remained uncoated while fibronectin- and collagen-coated wells were rinsed with PBS before the addition of 2.0 ml of a solution containing 5.0 µg/ml fibronectin (Sigma-Aldrich F0895) and 20.0 µg/ml collagen (Sigma-Aldrich C8919) diluted in PBS. Wells were then incubated for 1 h at 37°C before rinsing three times with PBS. For adipose-derived stem cell culture, wells were rinsed with PBS prior to 1 h incubation with 2.0 mL 25 µg/mL collagen (Sigma Aldrich C8919) dissolved in 0.1M acetic acid in ultrapure water at 37°C. Wells were then rinsed three times with PBS immediately prior to cell culture.

## **Materials and Cell Culture**

Cell culture media was obtained from the Cell Media Facility at the University of Illinois at Urbana-Champaign. Panc-1 cells, porcine adipose-derived stem cells, and neonatal rat cardiomyocytes were cultured in Dulbecco's modified Eagle's medium (DMEM) with 10% fetal bovine serum (FBS), 4 mM L-glutamine and penicillin-streptomycin. The HepG2/C3 cells were grown in minimum essential medium (MEM) with 10% FBS. PBS (pH 7.4) and poly-d-lysine (mol wt 70-150,000) were purchased from Sigma-Aldrich and trypsin (0.25% + EDTA) from Thermo scientific. Staurosporine was purchased from Sigma-Aldrich and dissolved in DMSO leading at a concentration of 1mg/ml.

All cell lines were grown in an incubator at 37°C and 5% CO<sub>2</sub> until 80% confluence and then passed using trypsin every 2-5 days as necessary. For imaging the cells were centrifuged to remove the trypsin and then resuspended in media and plated on the device in a total volume of 2 ml at a density of 4-6 x 10<sup>4</sup> cells/mL. Cell counting was performed with a hemacytometer (Reichert).

## **Cardiomyocyte isolation and culture**

Cardiomyocytes were obtained from 6-day old neonatal Sprague-Dawley rats (Harlan Laboratories, Inc.) using an approved protocol by the University of Illinois at Urbana-Champaign Institutional Animal Care and Use Committee (IACUC; Protocol #08190, Adopted from Maass et al., [12]). Briefly, whole hearts were excised from the rats and placed in 4°C HBSS buffer. Using small scissors, the left and right atria were removed and the remaining ventricles were quartered. The quartered ventricles were digested in 0.05% (w/v) purified trypsin (Worthington Biochemicals Corp.), while rotating gently at 4°C overnight. After 16 hours, warm growth medium was added for 5 minutes at 37°C to inhibit trypsin digestion. After washing and discarding the supernatant, 0.1% (w/v) purified type II collagenase (Worthington Biochemicals Corp.) was added for 45 minutes while rotating at 37°C. The tissue was gently triturated to mechanically loosen the cells, and the suspension was filtered through a 40-µm cell strainer. The suspension was removed after centrifugation at 150 x g for 6 min. The remaining cell pellet was re-suspended in warm growth medium and pre-plated for 1 hour to enrich for cardiomyocytes. The suspension was collected, and cardiomyocytes were seeded on polystyrene dishes. The growth medium consisted of high glucose (4.5 g/L) DMEM with 10% FBS. The cells were cultured in an incubator with 5% CO<sub>2</sub> at 37°C.

## **Porcine adipose-derived stem cell isolation**

Adipose-derived stem cells were isolated from back fat of pigs that were 3 months of age, in compliance with University of Illinois IACUC approved procedures. Pigs were euthanized by an overdose of pentobarbital and fat samples were excised from the back proximal to the spine. Adipose tissues were cleaned and submerged in PBS (without Ca or Mg) containing 3X Penicillin/Streptomycin prior to being cut into 1-2mm width strips. The strips were then minced and incubated on a shaker in 2.5 mg/ml solution of collagenase (Sigma, C2674) in PBS at 37°C for 2-3 hours. The resulting solution was

diluted 1:3 in PBS before centrifugation at 250 x g for 10 min. Floating adipocytes were removed and the remaining PBS aspirated from the cell pellet followed by resuspension and washing 2x in PBS. Red blood cells were removed by the addition of red blood cell lysis buffer (Sigma, R7757) for 2-3 minutes. Cells were then diluted with 30 ml PBS and centrifuged at 120 x g for 5 min, followed by aspiration of the supernatant and resuspension in 48 ml Dulbecco's modified eagle's medium (DMEM) with 10% fetal bovine serum. The resulting suspension was filtered twice through sterile gauze before additional centrifugation at 120 x g for 5 min and resuspension in 20 ml DMEM with 10% FBS. The cells were then filtered through a 100  $\mu$ m nylon cell strainer (Fisher, 22363549), prior to counting with a hemacytometer (Reichert). Cells were then plated at  $5-10 \times 10^3$  cells per  $\text{cm}^2$  in low glucose (1.0 g/L) DMEM with 10% fetal bovine serum prior to incubation in a low (5%)  $\text{O}_2$  incubator. Cells were cultured for 48 h prior to the first media change, and passaged at confluency. Cell aliquots were frozen at less than passage 5.

### **Porcine adipose-derived stem cell culture and differentiation**

Thawed ADSCs were cultured in low-glucose (1.0 g/L) DMEM with 10% FBS, penicillin-streptomycin, 2.9 g/L L-glutamine, and 0.2 g/L HEPES. Cells were cultured in an incubator maintained at 5%  $\text{CO}_2$ , 37°C. ADSCs were passaged no more than 5 times. For PCEM imaging, ADSCs were washed with PBS (without  $\text{Ca}^{2+}$ ,  $\text{Mg}^{2+}$ ), trypsinized using 0.25% trypsin (CellGro), and plated on PC biosensors in 2.0 ml at a density of  $5.0 \times 10^4$  cells/ml. To induce ADSC differentiation and development of dendrite-like cell projections, treated cells were exposed to a neurogenic induction medium containing 200 nM butylated hydroxyanisole (BHA), 2 mM valproic acid, 10 mM forskolin, 5mg/ml insulin, 2.5 mM KCl, and 25 mM hydrocortizone in solution with high-glucose (4.5 g/L) DMEM [16].

### **Statistical Analysis**

Two-tailed student's *t* tests were performed for the results described in Fig. 2-3 with *p* < 0.05 used to signify statistical significance. All *p* value determinations were two-tailed. GraphPad software (LaJolla, CA) was used for all calculations concerning statistical evaluation. Error bars indicate one standard deviation from the mean.

## **Results**

### **Dynamic Label-Free Imaging of Cell Attachment**

The imaging procedure is described in Figure 1 using HepG2/C3 hepatic carcinoma cells. Selected images are cropped and enlarged to show detail; cells were cultured on large ( $\sim 1.75\text{cm}^2$ ) sensor areas, and several 400  $\mu\text{m}$  x 400  $\mu\text{m}$  images were taken for each timepoint. To demonstrate the ability of this label-free assay to detect cell attachment at a

single-cell level, these images were cropped to the size of a few exemplary cells for the creation of each figure. The image shown in Figure 1a was recorded at an angle below both cell and background resonance conditions, and provides morphological information similar to traditional bright field microscopy. Red and blue circles in Fig. 1a mark the locations of pixels for which transmission intensity is plotted as a function of angle of incidence in Figure 1b. In Figure 1c, the final PCEM image displays AMT for each pixel as a function of position presented as a false-color composite. Cell attachment shifts the local resonance to a lower value as indicated by the red color. The bright field image, used in tandem with the PCEM image, can be used to correlate structural and morphological information with the cell attachment spatial distribution (Fig. 1d).

Comparison of the brightfield image with the PCEM image shows an increased footprint area in the PCEM image attributed to a combination of the formation of lamellipodia and by the ability of the cell to alter the AMT of PC regions directly adjacent to it. In a previous study, similarly configured PC biosensors demonstrated a detection resolution of 3.5  $\mu\text{m}$  in the direction parallel to the grating lines, and diffraction-limited resolution in the direction perpendicular to the grating lines [11] when an AMT shift 4x larger than those provided by typical cells was intentionally patterned on the PC surface with abrupt transition between high and low AMT. Based upon this earlier characterization, the cell attachment footprints measured by PCEM accurately reflect the cell boundaries within an uncertainty of  $\sim 2\text{-}3$   $\mu\text{m}$  in the direction parallel to the grating, and within  $\sim 1$   $\mu\text{m}$  in the direction perpendicular to the grating.

PCEM imaging is currently performed in a transmissive setup through the cell media, so it is likely that spatial resolution can be improved with the construction of a reflection-based detection instrument to avoid potential issues arising from sample-induced diffraction, scattering, and absorption. Scans completed in this study utilizes an incident angle scan range from  $1.5^\circ$  -  $2.0^\circ$  at  $0.01^\circ$  increments. As each image takes approximately 50 ms to collect, it takes approximately 30 s to collect and save the images required to build a PCEM image for one frame. The computation required to compose the final image requires an additional  $\sim 15$  s, allowing a final temporal resolution of approximately one frame per minute. As a result, cellular processes taking place on faster time scales may elude the PCEM processing modality in its current state, though scanning over a smaller range of angles or delaying image processing until conclusion of the study would result in moderate increases in sampling rate.

To demonstrate long-term application of PCEM, HepG2/C3 cells were plated on a poly-*D*-lysine (PDL)-coated sensor and the progress of their attachment was imaged via PCEM after 1, 2, 4 and 23 hours in culture. After one hour in culture, the HepG2/C3 cells show evidence of cell attachment, presenting average AMT shifts of  $0.25 \pm 0.01^\circ$  (1 S.D.) from background resonance. Throughout the time course, multiple changes in cell morphology can be seen in the bright field images, including changes in cell shape, size, and orientation throughout the experiment (Fig. 2). The PCEM images follow the changes in cell morphology observed in the bright field images, tracking the movement of the cell across the top of the field. Importantly, cells that translocate and cells that detach completely leave little to no evidence in the way of a footprint (Fig. 2, open arrows); this serves as further confirmation that the increased mass density causing AMT shift is

caused by the presence of proteinaceous cell attachments, and not merely material adsorption from culture media or cellular secretion. Similarly, as cells spread and create more pronounced attachments, areas of new attachment as indicated via brightfield microscopy show increased AMT shift via PCEM (closed arrows, Fig. 2). The relationship between PCEM images and bright field images lends PCEM extensive utility in tracking the relationship between dynamic cell activity and attachment footprint. At the 23-hour time point, PCEM images reveal that the cell areas interacting with the substrate are substantially larger than what may be inferred from bright field examination alone. Furthermore, the lateral resolution is sufficient to analyze variability of attachment within a single cell. The dark red color in the cell centers seen in the PCEM images indicates that attachment density is greatest at these locations.

### **Correlation with ECM-Dependent Physiologic Changes**

To demonstrate the ability of PCEM to resolve cellular changes in response to external stimuli, apoptosis was induced in Panc-1 human pancreatic cancer cells. Panc-1 cells were cultured on the sensor surface coated with PDL for 24 hours before treatment with 10 ug/ml staurosporine (Fig. 3). The morphological changes caused by staurosporine treatment are evident in the reduced definition of the cell border and rounded morphology shown in the bright field images. To characterize the cell response using PCEM, individual pixels were chosen from regions on the cell body (blue), on the cell periphery (green), and on the background (red). The selected regions are marked with circles on a bright field image and the curves for each pixel are given in the corresponding color in Figure 3a. Prior to treatment, the curves for both pixels on the cell body and the cell periphery overlap and display an AMT shift of  $0.10^\circ$  from background. After treatment, the pixel residing on the cell periphery presents a curve more closely resembling that of the background, indicating decreased protein density at this location. The cell body remains on the surface, but causes a smaller AMT shift from background, indicating a weakening of attachment. Finally, PCEM images display the decrease in attachment across the cell, as indicated by a lower AMT shift from background. This provides confirmation that cell attachment does not permanently alter the sensor surface but rather presents a transient increase in dielectric permittivity for the duration of cell attachment at that location on the biosensor.

Another interesting application of PCEM is concurrent monitoring of cell physiology, morphology, and attachment density. Cardiomyocytes require fibronectin-dependent integrin-mediated cell attachments for optimal development and contractility [12]. To verify that PCEM is capable of detecting significant differences in cell attachment caused by changes in the available ECM substrate, primary neonatal rat cardiomyocytes were isolated and cultured on an uncoated PC biosensor and on a biosensor coated with a combination of collagen and fibronectin [13]. At 24 hours the cells were imaged via PCEM, and their morphologies and contractility were recorded. Cells cultured in the absence of fibronectin showed greater frequency of rounded morphology, and showed a complete lack of contractility (Fig. 4a, 4b). Cells cultured in the context of both fibronectin and collagen, however, showed a significantly greater frequency of stretched morphology, and exhibited an increased proportion of contractile cells (Fig. 4b).

Additionally, contractility was exhibited only among cells showing a stretched morphology, supporting the fact that fibronectin-dependent cell attachment is critical for cardiac myocyte growth and differentiation are dependent on. AMT shift was evaluated over 70- to 100- pixel regions on and off each cell, enabling local background comparisons to be performed for each cell (see Supplementary Table 1 online). PCEM results confirmed the morphological observations, as cardiomyocytes exhibiting stretched morphology showed the greatest amount of AMT shift from background, and significantly greater amounts of AMT shift in comparison to their rounded counterparts, independent of the coating applied to the sensor surface (Fig. 4b,  $p = 0.0133$  and  $p < 0.0001$  for coated and uncoated sensors, respectively).

### **Characterization of Stem Cell Differentiation**

To demonstrate the capacity of PCEM for label-free assessment of cell differentiation, we exposed porcine adipose-derived stem cells to a neurogenic induction medium, performing PCEM before and after administration. The induced morphological changes are typical of neurogenic differentiation, characterized by retraction of the cell body and the development of small, dendrite-like cellular projections [14-15] (Fig. 4c). These changes were accompanied by a significant reduction in cell attachment as determined by a decrease in AMT shift (Fig. 4d,  $p = 0.0007$ ). As the neurogenic induction protocol stimulates remodeling of the cytoskeleton and cell attachments, decreased attachment protein density is to be expected. The agreement of PCEM with this assertion demonstrates that the technique can be used to characterize the progression of stem cell differentiation without disturbing the process with fluorescent labels or cytotoxic endpoint assays.

This work demonstrates several new capabilities of PC biosensors using PCEM. The technique is capable of visualizing dynamic cell attachment with a pixel resolution of less than one micron, enabling highly detailed quantification of attachment distribution within individual cells. The label-free aspect of PCEM enables the prolonged study of cell-ECM attachment evolution in the context of cell growth, locomotion, differentiation, and apoptosis. The ability to functionalize PC biosensors with multiple cell-amenable coatings allows the study of the effects of substrate composition on cell attachment. PCEM also allows direct comparison between bright field and PCEM images, enabling correlation of cellular morphology with changes in attachment density. This combination of capabilities provides a unique new tool for study of cell attachment in many contexts, including wound healing, cell culture optimization, stem cell differentiation, and cancer metastasis.

**Figure 2**

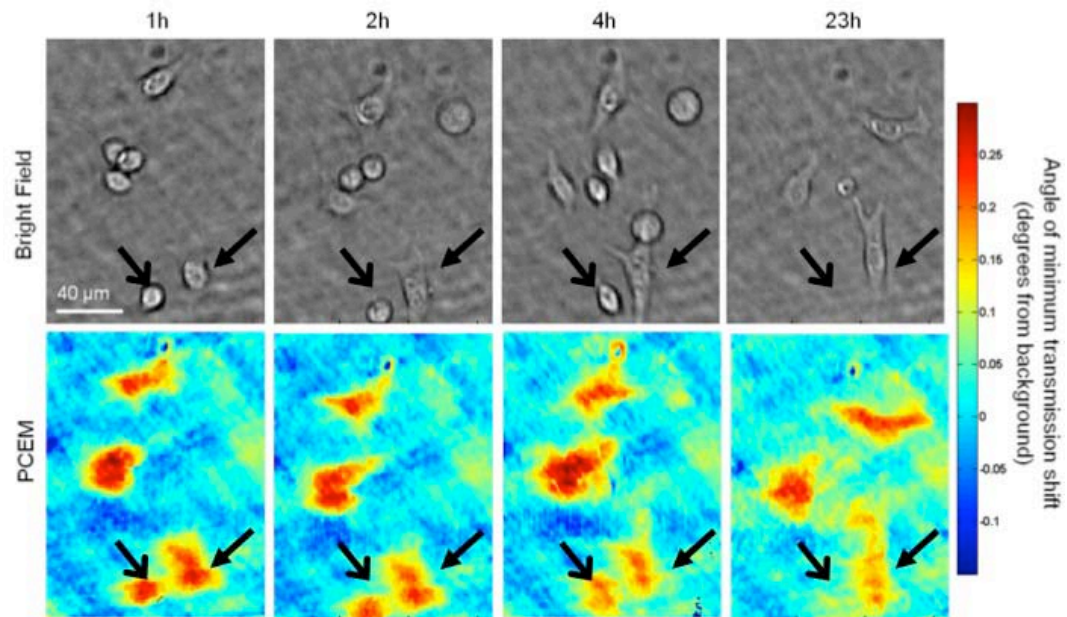


**Figure 2:** PCEM observation of cell growth and movement. HepG2/C3 hepatic carcinoma cell growth and locomotion were recorded over a 23-hour period via PCEM. The PCEM timecourse shows evidence of cell migration (closed arrow) as well as of cell detachment (open arrow).

**Figure 3**

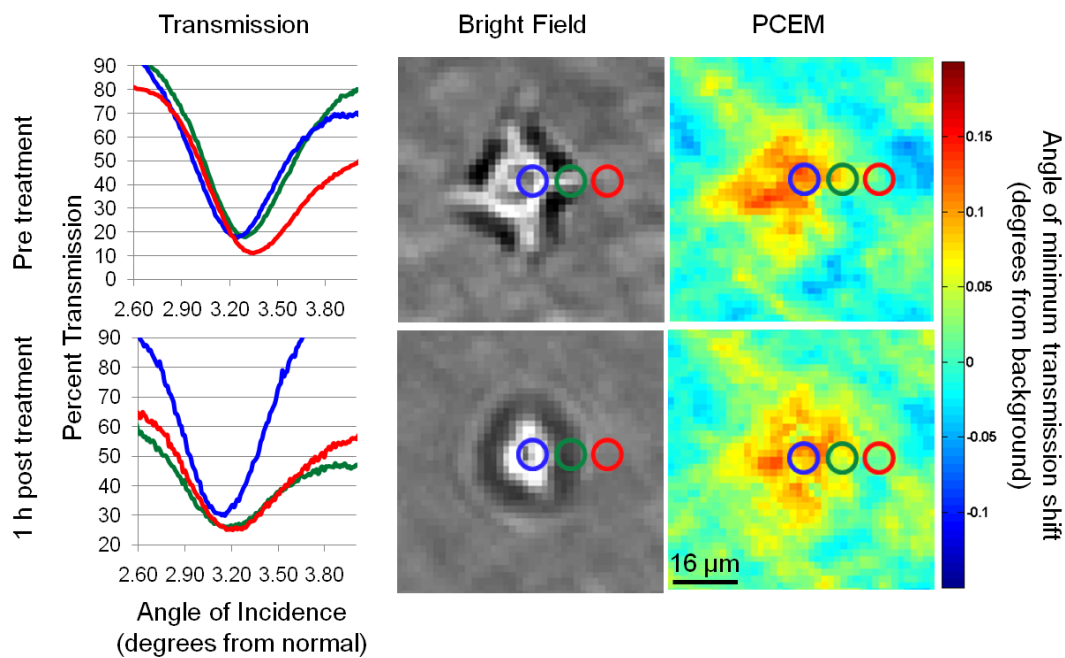


**Figure 3:** PCEM can be used to detect changes caused by apoptosis. Three individual pixels were chosen from regions on the cell body (blue), on the cell periphery (green), and outside the cell boundary (red). Intensity of transmission at is plotted as a function of angle of incidence. Curves generated for pixels on the cell body and the cell periphery overlap before treatment with staurosporine, indicating the presence of protein-dense cell attachments in these regions. PCEM shows decreased cell attachment after induction of apoptosis via staurosporine administration, and retraction of peripheral cell attachments (green) is supported by PCEM data.



**Figure 4:**

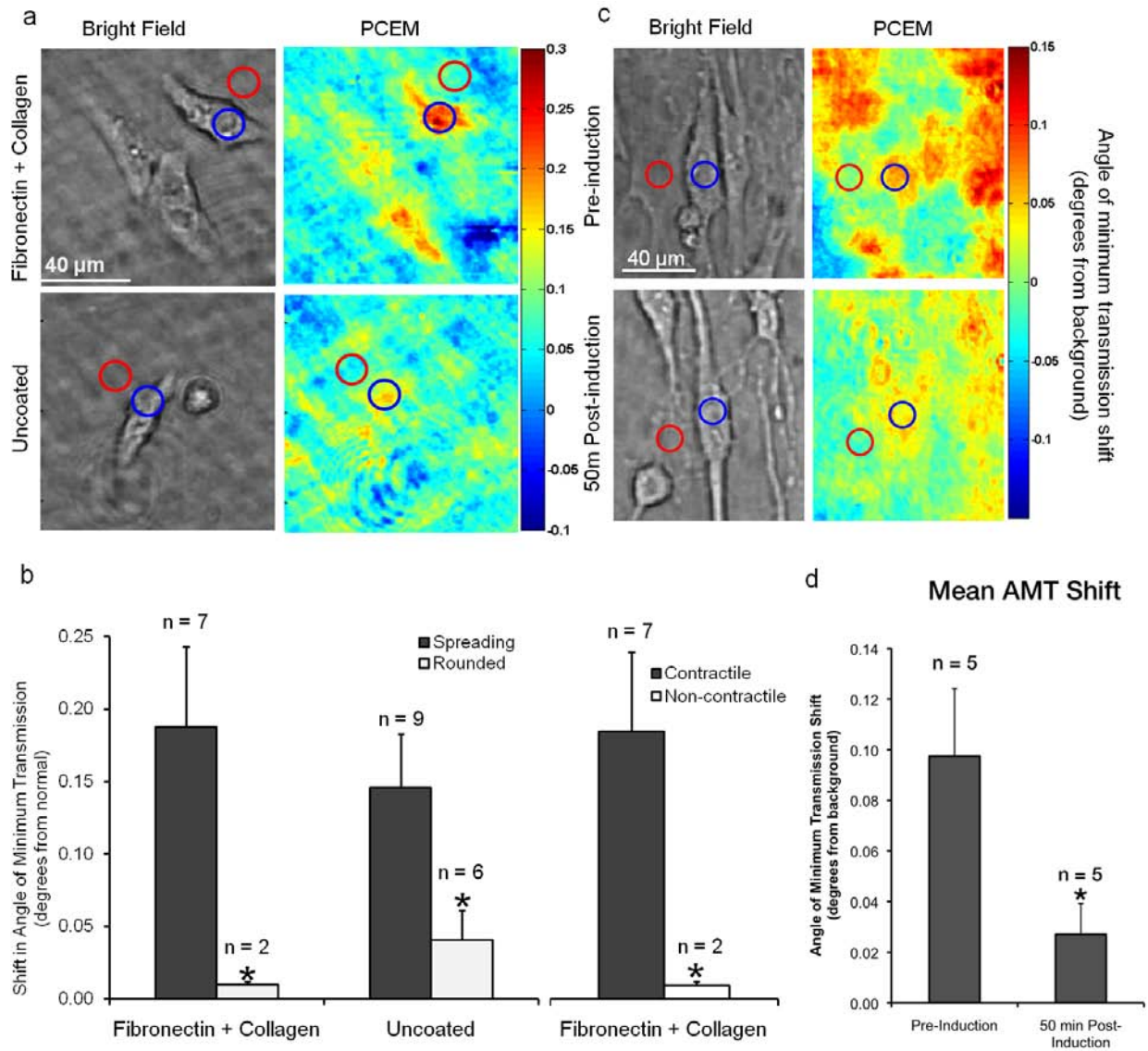


**Figure 4:** PCEM imaging of cellular responses brought about by extracellular stimuli. Blue circles indicate sample regions of interest used to measure AMT on individual cells, while red circles indicate sample regions of interest used to perform local background AMT measurements. a) Cropped bright field and corresponding PCEM images are shown for neonatal rat cardiomyocytes in culture on uncoated as well as fibronectin- and collagen-coated PC biosensors. b) On both coated (fibronectin + collagen) and uncoated sensors, cells exhibiting stretched morphology showed greater AMT shift than their rounded counterparts ( $p = 0.0133$  and  $p < 0.0001$ , respectively). Contractile cells also exhibited significantly greater AMT shift than non-contractile cells cultured on coated sensors ( $p = 0.0133$ ). c) Forced differentiation of porcine adipose-derived stem cells with neurogenic induction medium stimulates the production of dendrite-like cell projections

and retraction of cell bodies. d) Cells prior to treatment showed significantly greater attachment protein density than cells after treatment ( $p = 0.0007$ ).

### Label-Free Detection of Cell-Cell Signaling in Tumoral Immunity

While label-free optical biosensors have been used to detect cell attachment and cytokine signaling [7-8], there is currently no demonstration of label-free optical biosensing of cell-cell signaling. Cell-cell signaling is a crucial component of the immune response to invading pathogens as well as to control and inhibition of potentially threatening cells within the body. In a series of recent experiments, we have demonstrated that PC biosensors as a component of the SRU BIND<sup>TM</sup> system (Woburn, MA, USA) are capable of detecting interactions between cancer cell lines and immune cells. Briefly, several Responder cell lines (B2.1, HeLa, and RAW264.7) were cultured on PC biosensors and subjected to the addition of varying concentrations of Target (Jurkat T) cells. The Responders were monitored before, during, and after addition of the Target cells, and were observed to show significant differential responses for several combinations of cells. Notably, B2.1 Mouse Epithelial cells responded to the addition of apoptotic Jurkat T cells with a dose-dependent increase in peak wavelength value (PWV) shift, while addition of viable T cells elicited a negligible PWV shift with regard to media alone (Fig. 5). Positive results in this line of experimentation have encouraged further investigation of cell-cell signaling using PCEM; studies are currently underway to evaluate these interactions and other combinations of cell types at a sub-cellular resolution.

**Figure 5**

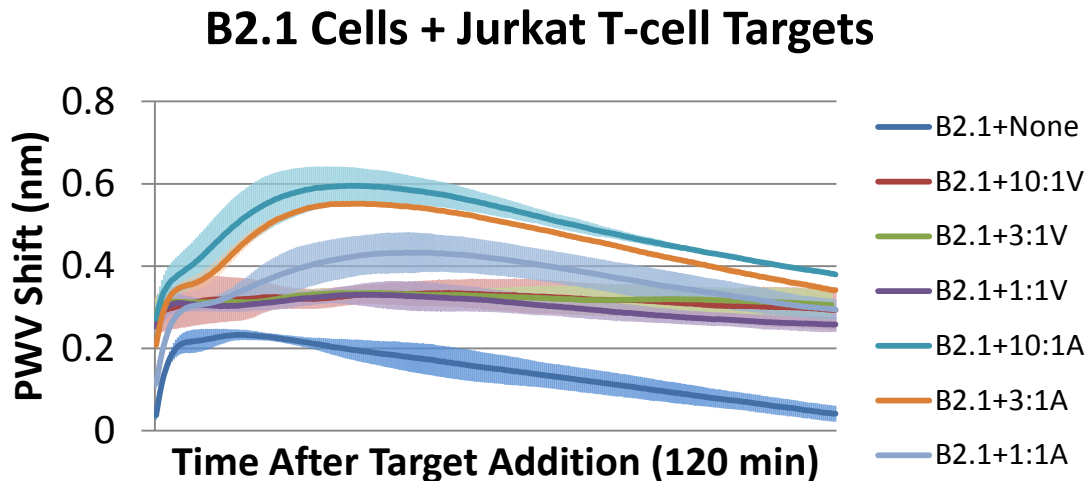


**Figure 5:** B2.1 Responder cells were cultured overnight on TiO BIND sensors before being monitored during and after addition of apoptotic and viable Target (Jurkat T) cells at 10:1, 3:1, and 1:1 Target:Responder ratios. Addition of viable cells elicited minimal change in PWV, while addition of apoptotic Jurkat cells caused a dose-dependent PWV shift as highlighted by the 10:1 teal, 3:1 orange, and 1:1 light blue curves above. Error

bars indicate 1 st. dev. above and below the mean of three replicates sampled for each time point.

We are currently seeking to improve our imaging capabilities using PC biosensors for label-free imaging of cell attachment. We are using several model systems, including Responder B2.1 (HEK clone) mouse epithelial cells, to test the ability of our sensors to resolve changes in cell attachment. Recent studies have indicated that our PC biosensor was not configured to achieve the best possible image (Figure 6).

To visualize physiologically relevant changes in cell attachment density, we treated Target Jurkat cells with actinomycin D to induce apoptosis, or with a vehicle control. We then added these cells to culture wells containing PC biosensors and B2.1 cells that had grown in culture overnight. Due to our previous PWV shift analysis on the BIND system, we expected that apoptotic cell addition would produce increased AMT shift with respect to addition of viable (vehicle-treated) cells. Although there appears to be a trend in this direction, the results are presently too noisy to establish a conclusive result (Figures 7,8).

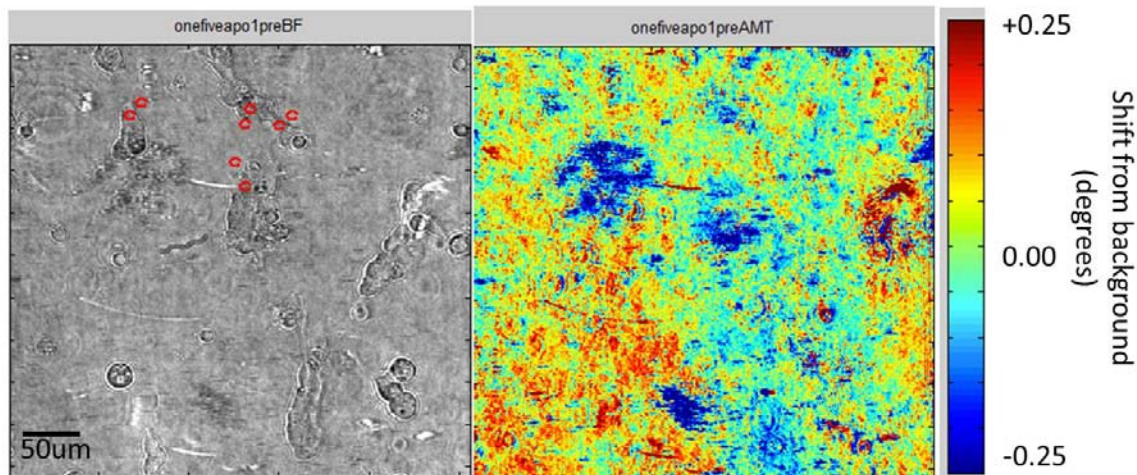


**Figure 6: High noise in PCEM images:** We have come to see predictable and elevated levels of noise from our updated PC biosensor structure, allowing for decreased spatial resolution with regard to cell attachment. Additionally, cells seem to produce a decrease in Angle of Minimum Transmission (AMT), when they should produce an increase in AMT due to the presumed elevated refractive index of the proteinaceous cell attachments in comparison to the surrounding media. Red circles indicate regions of interest for statistical analysis on and off the cell, before and after treatment.

We are currently working to achieve the best possible images from PC biosensors using transmissive imaging, but we are also pressing forward with two new imaging modalities as well. Over the coming months, we will be able to effectively decide the best method for using PC biosensors to conduct label-free imaging of cell attachment.

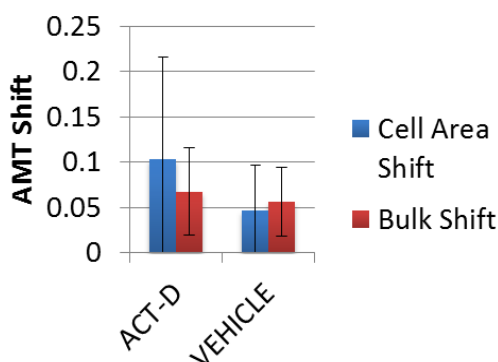


**Figure 7:** High variability in PCEM across imaging studies: PCEM results for the B2.1 Target:Responder experiment are favorable, but variability limits the utility of the study.

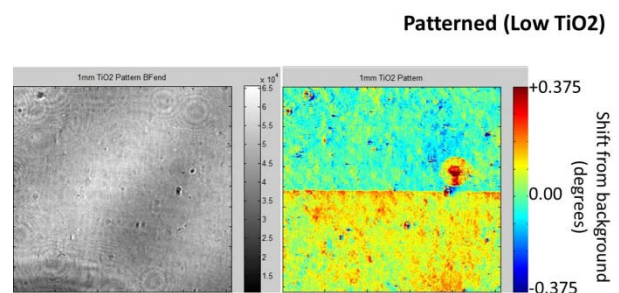


**Figure 8:** PCEM variability was further characterized by patterning a PC biosensor with high and low refractive index areas with SU-8, coating with additional TiO<sub>2</sub>, and then sonicating to remove the SU-8 pattern. As expected, the area with elevated TiO<sub>2</sub> (unpatterned) had an elevated AMT, while the area with reduced TiO<sub>2</sub> had a lower AMT. Variability, however, was still pronounced across the field, and along the order of shifts to be expected from cell attachment based on previous work.

To increase the performance of PC Enhanced Microscopy for physiologic changes in cell attachment density, it became imperative to overcome the background noise issue. After troubleshooting the image acquisition process, we were uncovered an unanticipated aspect of PC biosensors resulting in compromised performance of the peak-fitting algorithm employed to assess the resonance over the PC biosensor surface. Briefly, the biosensor is designed to have one peak reflected wavelength, resulting in a complimentary singular angle of minimum transmission (Lidstone et al. 2011). During the course of this analysis, we noted that over certain sensor areas, especially over cell boundaries, it is possible to elicit two or more dips in transmission, given a large enough range of angle tuning. By restricting the peak-fitting algorithm to search over a well-defined and characterized angle range, noise and imaging artifacts were substantially reduced (Figure 9).

Briefly, adherent HEK-clonally derived cells (B2.1) were cultured on PC biosensors overnight and analyzed for post-attachment shift (0 min) prior to the incubation with viable or apoptotic Jurkat T cells in suspension. Little to no change was observed in response to the addition of viable T cells (as expected), but significant and reproducible changes in cell attachment density were observed in response to the addition of apoptotic cells. This is due to the recognition (by B2.1 cells) of apoptotic residues on the Jurkat T cells. This experiment shows that by modifying image processing techniques, PCEM is capable of detecting physiologic changes in cell attachment on the order of single cells.



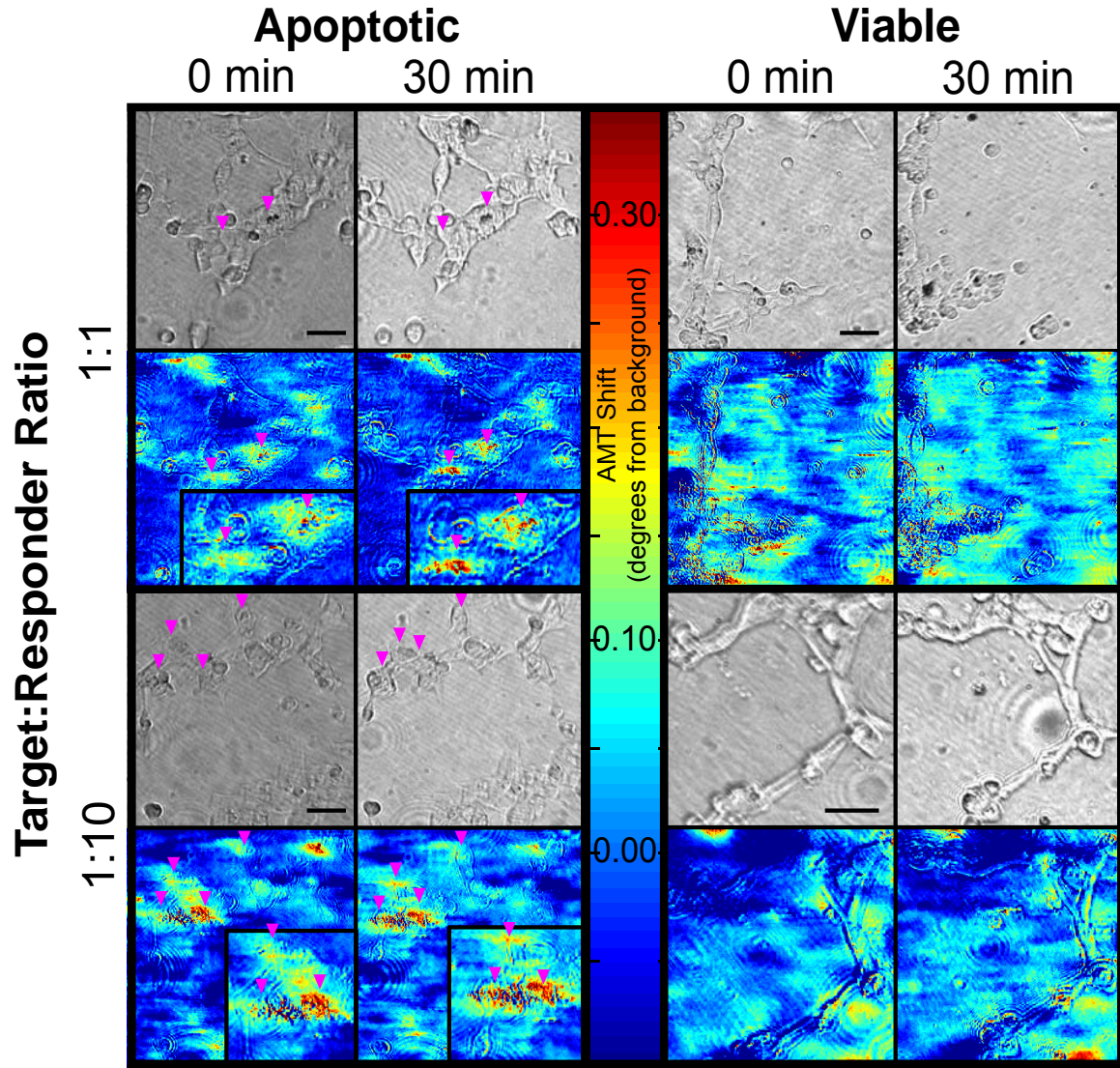


**Fig. 9:** Cell attachment density images recorded via PCEM, 30 min after B2.1 responder cells were exposed to apoptotic or viable targets. Bright field images (grayscale) represent bright field information, showing cell structure and morphology. PCEM data (heatmap) show elevated AMT shift w. r. t. background across areas of the sensor over which cell attachment has caused increases in mass density. As highlighted by the pink arrows and insets, certain cells show pronounced increases in cell attachment density, presumably from specific apoptotic recognition in response to Jurkat target cells. Scale bars represent 50 microns. Images were obtained using a 20X microscope objective over a 400x400-micron field of view, and were subsequently cropped and enlarged to enhance detailed

We have made significant advances in PCEM— most notably, modified peak analysis and image acquisition have enabled increased imaging performance for physiologic AMT shifts resulting from cellular activity on PC biosensors.

After establishing that long-term sensing is a viable option using PCEM, we will move on to test multiple ECM configurations in an effort to optimize the design of 3D scaffolds for cardiac myocytes. PCEM will not allow direct testing of three-dimensional substrates, so we will test the ECM proteins and concentrations of interest, and use the optimal

configuration for the construction of an ideal three-dimensional culture environment. The addition of this screening step in the design process will eliminate the time-consuming process of immediately committing all hypothesized ECM configurations to 3D tissue scaffolds for experimentation, while allowing us to establish trends in the factors governing cardiomyocyte growth and contractility at greater throughput.

#### **IV. KEY RESEARCH ACCOMPLISHMENTS**

- The utility of photonic crystal enhanced microscopy for the investigation and quantification of cell attachment has been demonstrated in a number of settings.
- The development of a new cell attachment evaluation technique will aid future studies involving cell attachment, from increasing tissue engraftment success rates to encouraging cardiac stem cell adhesion, growth, and differentiation.
- The proof of this technology in a biologically relevant context for basic science researchers

#### **V. REPORTABLE OUTCOMES (papers published or in preparation)**

- Label-Free Imaging of Cell Attachment with Photonic Crystal Enhanced Microscopy
  - *Analyst*, 2011, 136 (18), 3608 - 3615
- Label-free detection of cell-cell signaling between cancer and the immune system
  - In prep. for submission to the *Journal of Biological Chemistry*

#### **VI. CONCLUSION**

The importance and utility of label-free imaging have recently been underscored by an expansion in the number of techniques to acquire such data as well as by a growing need for improved understanding for a number of cellular processes. The use of fluorescent and chemical labels remains invaluable for the study of specific proteins and biochemical interactions, but the specificity such techniques provide often comes at the cost of decreased cell viability and a limited ability to study the same cells over extended periods of time. Such techniques also necessitate the use of one or several exogenous chemical markers in the area of interest within the cell, which introduces the possibility of obscuring the phenomenon of interest as it occurs in the absence of such labels. With the emergence of label-free techniques including surface plasmon resonance imaging (SPRi), ellipsometric microscopy, it has become possible to gain information complementary to that provided by traditional light microscopy. By decreasing the complexity of the experimental system, these techniques are in fact capable of investigating model systems with greater fidelity to their *in vivo* counterparts.

Despite this advantage, label-free imaging technologies continue to work against several challenges. While SPRi has enjoyed the ease of implementation associated with traditional surface plasmon resonance scanning techniques, one persistent area of difficulty is brought about by the lateral propagation of surface plasmons, which occurs on the order of several tens of microns [17]. This restricts the spatial resolution achievable with SPRi to distances on the order of entire cells, limiting the possibilities for its use in subcellular imaging. Similarly, ellipsometric imaging techniques have met with moderate success due to the comparatively small refractive index differences present in biological samples surrounded by aqueous media. PC biosensors seem to make several of

these problems more tractable – it is possible to construct PC-based sensors with propagation lengths of less than 5 microns, and sensors generally exhibit high sensitivity with regard to biological samples including proteins, nucleic acids, and whole cells immersed in aqueous media [4].

As the PCEM instrumentation registers shifts in transmitted wavelengths rather than changes in intensity, PCEM remains insensitive to the detection of particles passing transiently through the field of view. This represents another advantage over intensity-based detection assays, which may demonstrate susceptibility to artifacts in the presence of soluble particles capable of absorbing wavelengths of interest for analysis. Materials that adsorb to the sensor surface that also strongly absorb light at the laser wavelength have been documented to extinguish the PC resonance. In such a case, the resonance disappears, and the AMT fitting algorithm no longer functions [18]. Such regions can be automatically recognized by the instrument software. Although no such cases were observed for the experiments conducted in this work, this technique has been used to measure deposition of light-absorbing hydroxyapatite produced by surface-attached stem cells that have differentiated to become osteoblasts.

In this work, we demonstrated PCEM as a useful tool to study a number of biologically interesting questions regarding cell attachment in several contexts. Because this new technique grants access to previously unavailable information, it will allow the achievement of a greater level of understanding not only in fundamentally interesting areas of cell biology, but also clinically relevant questions such as what types of cellular changes enable cancer metastasis, and what kinds of biomaterials and biocompatible polymers might best be applied to increase wound healing and recovery in the absence of inflammation and scarring. Questions such as these will require an unprecedented understanding of the extracellular matrix as well as of the cells interacting with that ECM. In future work, PCEM may be used in combination with existing technology to increase our understanding of the biology underlying problems like cancer metastasis, wound healing, axonal repair, and ischemic damage. The combination of PCEM with specific fluorescence labeling, for example, will allow the investigation of individual protein and signaling interactions in such contexts with respect to their influence on cell attachment. Modeling disease systems and using recently developed biomaterials on PC biosensors with this new technique will allow new insight into these problems, enabling researchers to develop more successful therapeutic approaches to clinical disease.

## VII. REFERENCES

1. Boudreau, N.J., Jones, P.L., *Biochem. J.* (1999) 339, 481±488
2. Barczyk, M., Carracedo, S., Gullberg, D. *Cell Tissue Res.* 2010 Jan;339(1)269-80.
3. Cunningham, B.T., Li P., Lin B., Pepper, J. *Sens. Act B: Chem.* 81(2-3)316-328, 2002.



4. Cunningham, B.T. *et al. J. Biomol. Screen.* 9(6)481 – 490, 2004.
5. Li, P.Y., Lin, B., Gerstenmaier, J. Cunningham, B.T. *Sens. Act. B* 99:6-13, 2004.
6. Chan, L., Gosangari, S., Watkin, K., Cunningham, B.T. *Apop.*, 12(6)1061-1068, 2007.
7. Petersen, A.W., Halter, M., Tona, A., Bhadriraju, K., Plant, A.L., *BMC Cell Biol.* 10:16, 2009.
8. Yanase Y *et al. Biosens Bioelec.* 26 (2010) 674–681, 2010.
9. Bivolarska, M., Velinov, T., Stoitsova, S. *J. Micros.* 224(3)242-248, 2006.
10. Marinkovaa, D., *et al. Coll. Surf. B: Biointer.* 65:276–280, 2008.
11. Block, I.D., Mathias, P.C., Jones, S.I., Vodkin, L.O., and Cunningham, B.T., *App. Optics* 48(34)6567-6574, 2009.
12. Block, I.D., Mathias, P.C., Ganesh, N., Jones, S.I., Dorvel, B.R., Chaudhery, V.C., Vodkin, L.O., Bashir, R., and Cunningham, B.T. *Optics Express* 17(15)13222-13235, 2009.
13. Mikson, A., Ehashi, T., Mahara, A., Uyama, H., Yamaoka, T., *J. Artif. Org.* 12(2):111-117, 2009.
14. Maass, A.H., Buvoli, M. *Meth. Mol Biol.* 366:321-30, 2007.
15. Safford, K.M. *et al. Biochem. Biophys. Res. Comm.* 294(371-379), 2002.
16. Huang, T., He, D., Kleiner, G., Kuluz, J. *J. Spinal Cord Med.* 30(S1:S35-40), 2007.

17. Caldwell M.E., Yeatman E.M. *App. Optics* 31(20)3880-289, 1992.

18. Shamah, S. and Cunningham, B.T. *Analyst* 136(1090-1102)

## Section 2. Distributed Feedback Laser Biosensor Noise Reduction

In this Progress Report, We report on a signal processing approach that enables detection of lasing wavelength shifts as small as  $\Delta\lambda \sim 1.5\text{pm}$  from a distributed feedback laser biosensor (DFBLB) fabricated upon a plastic substrate and incorporated into microplates. In this work, we study the effects of the three approaches on the low-noise measurement of lasing wavelength from a plastic-based DFBLB in microplate format. We first apply a fitting coefficient to automatically exclude emission spectra that deviate from a Lorentzian model and examine the influence of the external pump repetition rate. We also compared the noise calculated from temporally averaged measurements. Using all three approaches together, we are able to reliably measure wavelength shifts as small as 1.5 pm, as determined by  $3\sigma$  ( $\sigma=0.5$  pm). Dose-response characterization is performed for a protein-protein interaction, in which immobilized Protein A is used to capture an antibody from a test sample.

### *Single-mode Operation Determination*

Optical pumping of the DFBLB generally results in single mode lasing output, with a spectral characteristic measured by the spectrometer that can be fit to a Lorentzian function. The lasing wavelength value (LWV) for a biosensor measurement is defined as the wavelength of peak output intensity. However, deviations of the actual lasing spectrum from the Lorentzian curve are often observed as shown in the inset of Figure 1, where more than one lasing mode is present. The curve-fitting algorithm, unable to match the data to the expected Lorentzian function, reports a LWV that is no longer representative of the actual lasing wavelength. Therefore, it is necessary to introduce a quantity to describe how well the measured spectrum represents a classical Lorentzian profile, and a threshold for rejecting spectra that will result in elevated LWV noise. Here, we use the coefficient of determination ( $R^2$ ) as defined by  $R^2 = 1 - \text{SS}_{\text{err}} / \text{SS}_{\text{tot}}$ , where  $\text{SS}_{\text{err}}$  is the sum of squares of residuals and  $\text{SS}_{\text{tot}}$  is the total sum of squares. Figure 1 demonstrates the calculation of  $R^2$  for several representative spectra. We have selected a threshold value of  $R^2 > 0.8$  for a sensor spectrum to be considered acceptable for further analysis. If a sensor begins to demonstrate multimode output behavior, the algorithm automatically identifies it, and flags the sensor so its output may be disregarded.

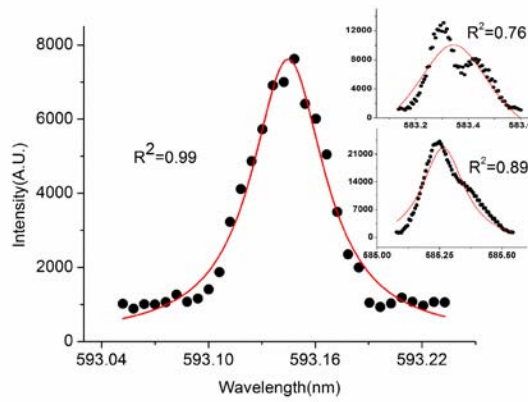


**Fig 1.** Fitted spectra of DFBLB output displaying either single mode or double mode operation..

### ***Pump Repetition Rate***

To study the effect of pump repetition rate, the integration time for the spectrometer was set to 500 ms and pumping rates of 1 Hz, 3 Hz, 6 Hz, and 10 Hz were compared. For each pump rate, the standard deviation ( $\sigma$ ) was calculated from 85 discrete measurements. The inset of Figure 2 compares the dynamic LWV readout over time sequences with pump rates of 1 Hz and 10 Hz. We observe that the noise amplitude decreases with increasing pump rate, as a single gathered spectrum is comprised of the combined output of a greater number of pulse outputs within a fixed duration, resulting in a more pronounced “peak” in the measured spectrum. This effect is further confirmed through changing the integration time of the spectrometer (400 ms and 600 ms), as shown in Figure 2. A further observation is that the noise decreases as the integration time is increased for a fixed pump rate, which indicates that the gathered spectrum can be fit more accurately as the more outputs are accumulated. Beyond an integration time of 600 ms and pump rate of 10 Hz pumping, the noise is not reduced further.

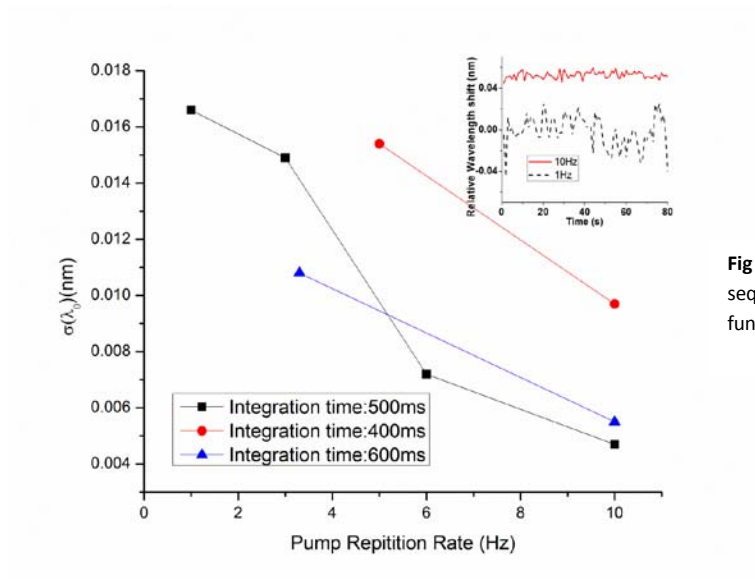


**Fig 2.** The standard deviation ( $\sigma$ ) calculated from a sequence of independent measurements plotted as a function of the external pumping repetition rate.

### ***Boxcar averaging and Protein A-IgG Binding***

To further reduce noise, a boxcar method was studied. The boxcar method can reduce noise by  $\sqrt{N}$ , where the noise is characterized by the standard deviation  $\sigma$  calculated from the multiple independent measurements. Boxcar averaging was applied to the data using  $N \leq 10$ . The integration time of the CCD was set to 500 ms and the external pump rate was 10 Hz. The black curve in Figure 3 shows that the noise decreased from  $\sigma=4$  pm to  $\sigma=0.5$  pm as the boxcar number  $N$  increased from 1 to 10. The inset of Figure 3 illustrates the dynamic variation of the averaged lasing wavelengths. We observe that determination of the lasing wavelength is improved by temporal averaging. However, such improvement results in a dramatic decrease in the scanning speed required for gathering kinetic data, as a boxcar length of  $N=10$  corresponds to 50 pulses gathered over a time span of 5 seconds. This approach was applied to the dose-response characterization of the interaction between an immobilized protein and an analyte protein in solution.

Protein A was attached to the DFBLB surface using covalent bonds by functionalizing the sensor surface aldehyde-based surface chemistry. The shift from Protein A adsorption was  $\Delta\lambda=0.67 \pm 0.05$  nm. After Protein A was immobilized on the sensor, it was exposed to a rabbit antibody under a range of concentrations (17, 3.4, 0.68, 0.34  $\mu\text{M}$  and 68, 34 nM). Figure 4 (a) shows the laser wavelength shift end point as a function of rabbit IgG concentration. The detected signal for the high concentration (17 $\mu\text{M}$  rabbit IgG) approaches saturation due to the limited number of protein A binding sites on the sensor surface. The lowest concentration of rabbit IgG (34 nM) resulted in an easily measured laser wavelength shift of  $\Delta\lambda=50$  pm. Using

nonlinear curve fitting to determine the inflection point of the dose-response curve, we measured a dissociation constant of  $K_d=0.53 \mu\text{M}$  for the protein A-IgG interaction, which corresponds well with reported values [3].

Fig 3. The standard deviation ( $\sigma$ ) calculated from a sequence of independent measurements plotted as a function of the external pumping repetition rate.

Fig 4. (a) The laser wavelength shift end point as a function of rabbit IgG concentration for DFBLB sensors prepared with capture Protein A. The error bars represent the standard deviation from three replicate experiments from separate sensors. (b) The detection kinetics for human IgG at 34nM with spectra measured every 8 s.

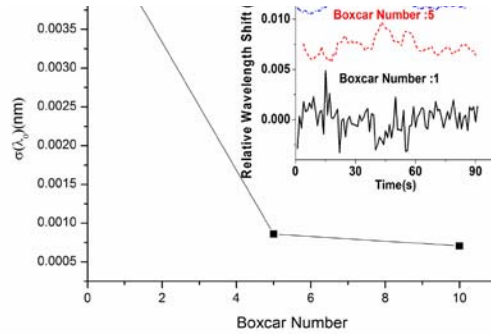
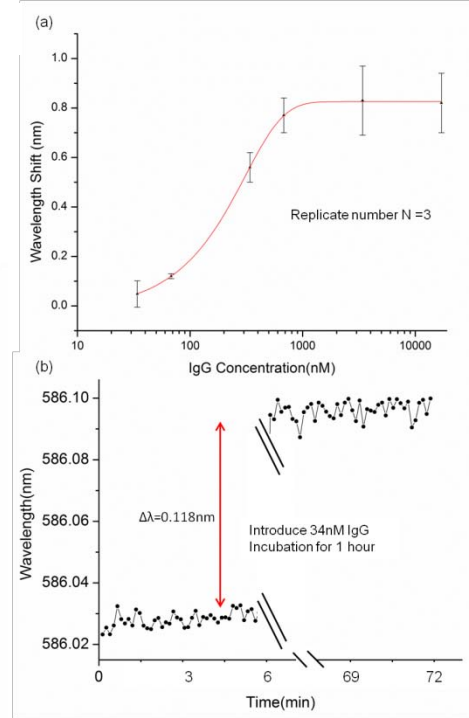


Fig 4.



## Summary

In this work, we have demonstrated how a combination of detection instrument configuration and data analysis can be used to obtain low noise from DFBLB sensor measurements. Detection of wavelength shifts as small as 1.5 pm is demonstrated, which satisfies the requirement for characterization of protein-protein interactions, as demonstrated using the Protein A-IgG system.

### **Section 3. External Cavity Laser Biosensor**

Since the first demonstration of surface plasmon resonance as a label-free optical biosensor, there has always been a desire to pursue high sensitivity, high resolution, robust, and inexpensive detection approaches based upon the properties of optical resonators to extend the limits of detection of label-free assays to lower concentrations and to increase the signal-to-noise ratio for observation of lower concentrations or smaller molecules. Recently, utilizing a tunable photonic crystal (PC) resonant reflector as the wavelength selective element of an external cavity laser (ECL) cavity, we have demonstrated a novel single-mode continuous-wave narrow bandwidth emission and widely tunable external cavity laser biosensor, representing a fundamentally different approach to the problem of achieving high  $Q$ -factor resonance and simultaneously high-sensitivity for label-free resonant optical biosensors. This novel ECL biosensor enables simple optical coupling and a sensor format that is amenable to high-throughput multiplexed analysis for a broad array of applications in life science research, pharmaceutical screening, diagnostics, and environmental monitoring.

#### **External cavity laser label-free biosensor based on PC resonator: Design**

Since the first demonstration of surface plasmon resonance (SPR) as a label-free optical biosensor<sup>1</sup>, research in the field of high sensitivity, high resolution, robust, and inexpensive detection approaches based upon the properties of optical resonators has been very active, but has resulted in commercial implementation of only a few approaches. Applications in pharmaceutical high-throughput screening, pathogen detection, and life science research all demand a challenging combination of low cost (for both sensor fabrication and detection instrumentation), robustness (not requiring the user to perform optical alignment of components), high sensitivity, resolution (for detection of analytes at low concentrations or detection of small molecule analytes binding to large proteins), and high-throughput (the ability to perform a large number of independent assays in parallel). Label-free detection of biomolecules and biological particles, such as cells, virus, and bacteria, has been an area of intense research and commercial development, as it enables detection of analytes through their intrinsic physical properties, rather than indirect detection of artificially introduced labels or stains. The main benefits of label-free assays are simplified assay procedures, the ability to gather kinetic data, and the possibility of studying biomolecular processes without the physical effects of labels on binding - such as epitope blocking, steric hindrance, and label-induced conformational changes.

A tremendous number of label-free assays for every conceivable type of biological analyte have been demonstrated<sup>2,3</sup>. Yet, there has always been a desire to extend the limits of detection of label-free assays to lower concentrations and to increase the signal-to-noise ratio for observation of the lowest concentrations or the smallest molecules.

Here, we describe for the first time an alternative label-free optical biosensor approach that achieves high resolution while maintaining high sensitivity. The novel element of our approach

is utilization of optical gain, so as to realize an active optical cavity that achieves narrow bandwidth continuous wave light output via the process of stimulated emission. We use a photonic crystal resonant reflector surface as the transducer upon which biological material is adsorbed, which also serves as one mirror of an external cavity laser (ECL). As shown in Figure 1, an optical fiber-coupled semiconductor optical amplifier (SOA) is used as the gain media, which illuminates the PC at normal incidence. The PC reflects a narrow band of wavelengths through the optical fiber, and back into the SOA to establish a laser cavity whose emission wavelength is tuned by the adsorption of biomaterial on the PC surface. Importantly, the smooth gain spectrum of the SOA and the length of the external cavity (determined by the length of the optical fiber), result in apparently continuous tuning of the lasing wavelength without abrupt hops between modes. A rough means for comparing performance between resonant optical biosensors is to calculate a figure of merit (FOM) that incorporates the sensitivity of the sensor (the magnitude of a measured quantity change) and the resolution for measuring small changes in that quantity. The FOM of this approach ( $2.8 \times 10^7$ ) is 100 greater than PC biosensor ( $2.1 \times 10^5$ ).

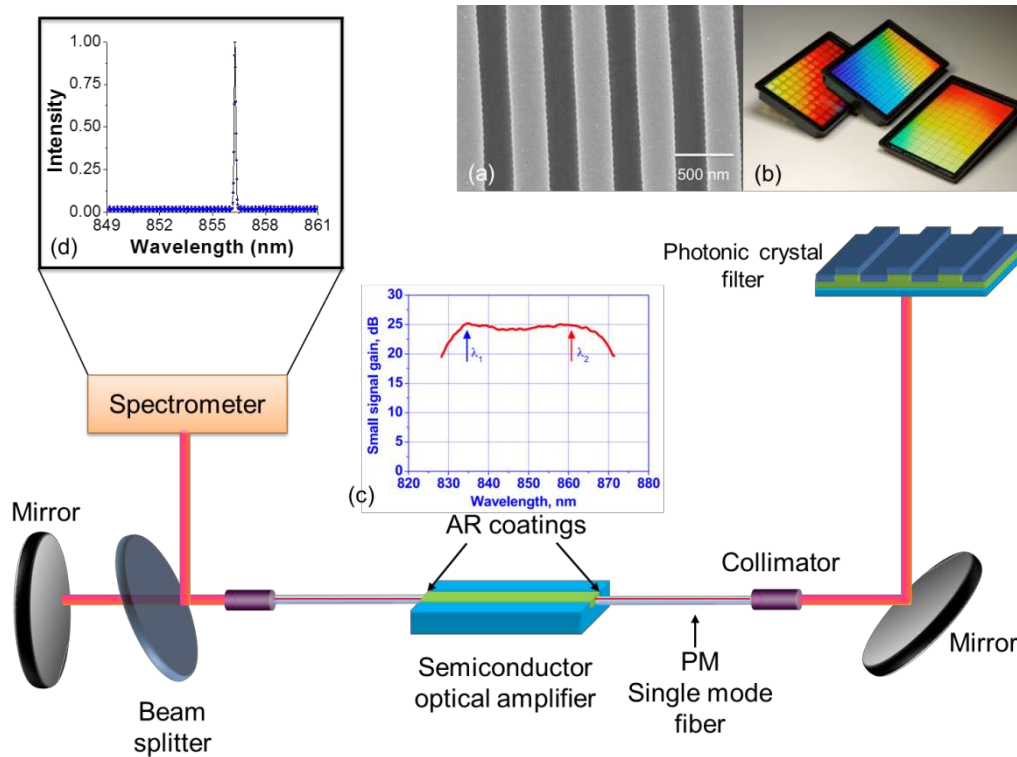


**Fig.1.** Schematic of the external cavity laser biosensor system. Inset a: Cross-section scanning electron micrograph (SEM) image of the PC structure fabricated by the nanoreplica molding process. Inset b: PC resonator in standard microplate-based formats. Inset c: The small signal gain spectrum of the SOA. Inset d: A typical lasing spectrum of the PC based ECL.



The sensor surface is a 1-dimensional surface PC comprising a low refractive index, ultra-violet curable polymer (UVCP) periodic grating ( $\Lambda = 550$  nm,  $t_{\text{grating}} = 170$  nm) that is coated with a high refractive index thin film of  $\text{TiO}_2$  ( $n = 2.35$ ,  $t_{\text{TiO}_2} = 120$  nm) that is designed to provide a resonant reflection near  $\lambda_0 = 855$  nm when covered with water. The PC is fabricated on a flexible plastic substrate using nanoreplica molding to form the grating structure, using fabrication methods described in our previous work<sup>4</sup>. Importantly, the PC sensor surface can be inexpensively manufactured over large surface areas to produce biosensors in a standard microplate format, for compatibility with automated liquid handling formats used for applications that require high throughput.

The detection instrument comprises an SOA, two polarization maintaining single mode optical fibers, a near-infrared (NIR) mirror, and an instrument for measuring laser wavelength. The SOA used in our work (SAL-372, Superlum Inc., center wavelength of  $\lambda_0 = 850$  nm and a 3-dB bandwidth of  $\Delta\lambda = 40$  nm) has both edge facets coated with antireflective (AR) layers ( $R < 10^{-3}$ ) with a tilted waveguide design to obtain a gain ripple as low as 0.2 dB<sup>5</sup>. Each end facet of the SOA is coupled to a single mode polarization maintaining fiber with a length of 1 m.

The output of one side of the SOA is reflected against a mirror, while the other end directs light through a collimating lens against the PC at normal incidence. A portion of the lasing emission is directed by a 98:2 beam splitter to a detection instrument such as a spectrometer or interferometer. Theoretically, the ECL biosensor system's detection limit is ultimately set by the mode density or the free spectral range (FSR) of the ECL cavity. The cavity mode spacing is

given by 
$$\Delta\lambda_m = \frac{\lambda^2}{2(n_0 l_0 + n_g l_g + n_{SOA} l_{SOA})}$$
, where  $m$  is the mode number,  $\lambda_m$  is the  $m^{\text{th}}$  resonant wavelength,  $\lambda$  is the center wavelength, and  $n_0$ ,  $n_g$ ,  $n_{SOA}$ ,  $l_0$ ,  $l_g$ ,  $l_{SOA}$  are the effective refractive index and optical length of the air, single mode fiber, and the SOA cavity, resulting in a cavity length that is dominated by the length of the optical fiber. By using two 1 m single-mode fibers, a longitudinal mode spacing of 0.08 pm is estimated, representing the smallest increment in wavelength shift that can be obtained.

As the ECL biosensor resonates, high intensity electromagnetic standing waves are established at the PC-media interface. Adsorption of biomolecules on the PC tunes the resonant wavelength of the PC, which subsequently tunes the emission wavelength of the ECL. While the PC is a passive optical resonator with modest  $Q$ -factor ( $Q \sim 1000$ ), its interaction with the gain provided by a semiconductor optical amplifier through the formation of a resonant cavity results in an active optical resonator with an extremely high  $Q$  ( $Q \sim 2.8 \times 10^7$ ) through the stimulated emission process, while retaining high sensitivity. The ECL biosensor generates single-mode, continuous-wave laser emission whose wavelength is tunable over a wide range by adsorption of biomaterial on the surface of the PC, and thus exhibits large dynamic range. The arrangement combines the high sensitivity of the PC passive resonator with the high resolution of the external cavity laser emission.

## External cavity laser label-free biosensor based on PC resonator: Characterization

The reflection spectrum of the PC, the spontaneous emission spectrum of the SOA, and the laser emission spectrum of the ECL-PC are shown together in Figure 2(a). The PC exhibits a resonance peak with a 3-dB bandwidth of  $\Delta\lambda = 2$  nm. Using a spectrometer to measure the ECL emission spectrum (IHR550, Horiba Jobin Yvon), the width of the lasing peak is at least as narrow as  $\Delta\lambda = 30$  pm, as limited by the wavelength resolution of the spectrometer. In order to more accurately measure the Q, a scanning Fabry-Perot cavity interferometer with a resolution of 7.5 MHz was used. The interferogram is shown in Figure 2(b-c). Figure 2(b) is an FSR plot, which is used to calibrate the time-base of the oscilloscope. A Q-factor ( $\lambda_0/\Delta\lambda$ ) of  $2.8 \times 10^7$  is determined at a center wavelength of  $\lambda_0 \sim 853$  nm. The relationship between the laser output power and the injection current is shown in Figure 2(d), demonstrating a threshold current of 48 mA and a slope efficiency of 39 mW/A at 20 °C.

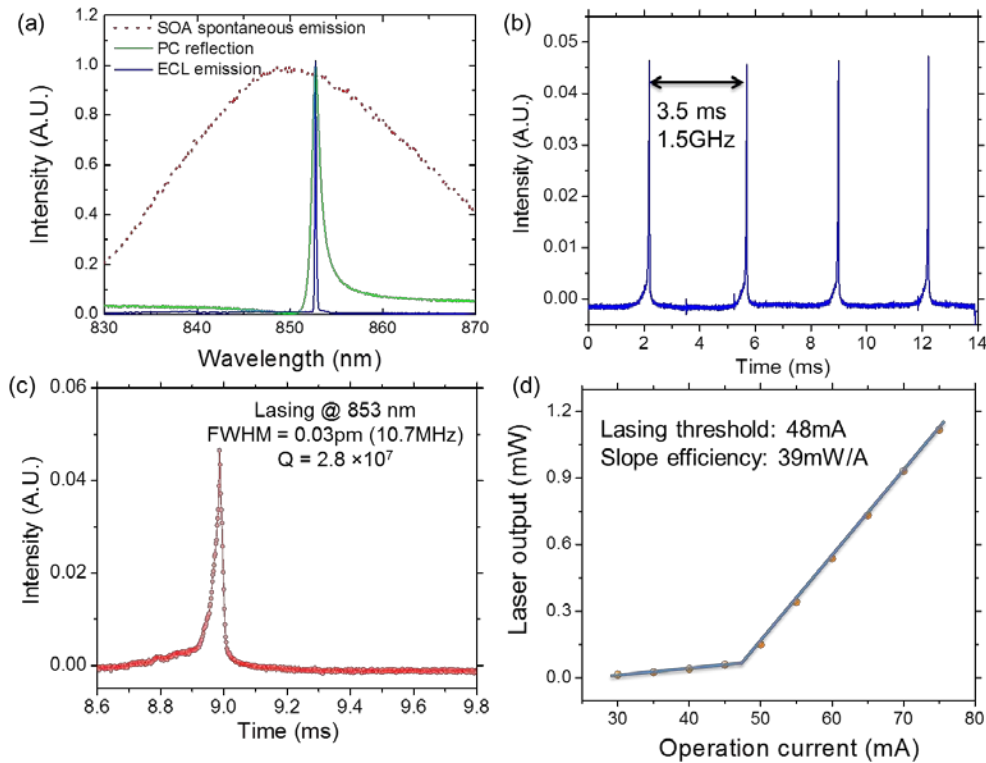


**Fig.2.** Lasing characterization. (a) Overlaid SOA spontaneous emission spectrum, PC resonant reflection spectrum, and ECL single mode emission spectrum. The red dotted curve displays the spontaneous emission spectrum of the SOA obtained under an injection current of 56 mA at 20 °C. The green curve represents the PC resonant reflection spectrum and the blue curve denotes the ECL lasing spectrum. (b) (c) Interferogram. ECL emission spectrum measured using a scanning Fabry-Perot interferometer with 7.5 MHz resolution. (b) FSR Plot. Knowing the FSR of the interferometer is 1.5 GHz, the calibration factor is found by setting 1.5 GHz = 3.5 ms

(428.57 MHz/ms), the distance between the two peaks. With the oscilloscope timebase calibrated from the inset plot, the FWHM of the laser emission is determined to be  $0.025 \text{ ms} \times 428.57 \text{ MHz/ms} = 10.71 \text{ MHz}$ , which corresponds to a FWHM = 0.03 pm in wavelength. (c) shows a close-up of the actual signal of the laser, which results from the convolution of the laser linewidth and finesse of the interferometer FP cavity. (d) The light vs. current (L.I.) curve associated with the external cavity laser. Using a linear least-squares fit to the emission fluence above threshold, clear threshold current of 48mA and slope efficiency of 39 mW/A are found.

In order to characterize the bulk refractive index sensitivity of the sensor and to demonstrate single-mode lasing operation over a large wavelength range, PC surfaces were exposed to a series of liquid samples with the solvent dimethyl sulfoxide (DMSO) mixed with water. The refractive index ( $n$ ) of the liquids ranged from 1.333 to 1.395 (at  $\lambda_0 = 860 \text{ nm}$ ). The lasing spectrum, gathered by the spectrometer, was fit to a Lorentzian function, and the lasing wavelength was determined by mathematically determining the peak wavelength of the Lorentzian. The corresponding laser wavelength shifts (LWS) are shown in the inset plot of Figure 3 resulting in a linear bulk refractive index shift coefficient of  $S_b = 212 \text{ nm/RIU}$  over a dynamic range of 13 nm. The full operating range of the system is limited by the gain spectrum of the SOA, which can provide gain in the  $830 < \lambda < 870 \text{ nm}$  range.

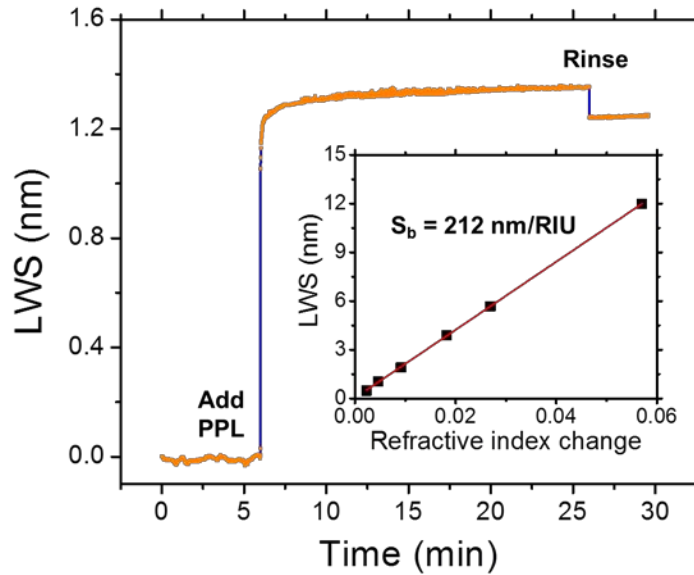


**Fig.3.** ECL sensor characterization. Inset: Bulk sensitivity characterization. Laser emission wavelength shifts of the sensor exposed to liquid media with different refractive index. A linear fit to the experimentally obtained data reveals a bulk sensitivity of 212 nm/RIU. Main figure: Surface sensitivity characterization. Kinetic

plot of polymer protein self-limiting monolayer (PPL) absorption induced laser emission wavelength shift.

By monitoring the spectral output of the ECL biosensor as a function of time, the kinetic characteristics of surface mass adsorption can be recorded. Figure 3 illustrates the dynamic detection of the growth of a single protein polymer poly-(Lys, Phe) (PPL, Sigma–Aldrich) monolayer (thickness  $\sim 15$  nm<sup>6</sup>) with independent wavelength measurements taken with a time interval of 500 msec. These data were obtained by initially establishing a baseline emission wavelength when the PC surface was covered with a phosphate-buffered saline (PBS) solution with pH = 7.4. After 6 minutes, the PPL solution was added (0.5 mg/ml in PBS) and stabilized for 20 min, followed by rinsing of the surface with PBS to remove any PPL that was not firmly attached. PPL has been demonstrated to form a self-limiting single monolayer coating upon dielectric surfaces<sup>6</sup>. The sensor exhibited an emission wavelength shift of  $\sim 1.24$  nm for PPL monolayer adsorption, and no drift of the lasing wavelength was detectable over time periods up to one hour.

A conventional demonstration for characterizing the ability of a sensor to observe small molecule adsorption is the detection of biotin (Molecular weight (MW) = 244 Da) by an immobilized capture layer of the protein streptavidin (SA, MW = 60,000 Da). The biotin-SA interaction displays one of the strongest binding affinities found in nature ( $K_d = 10^{-15}$  M), and each immobilized SA molecule is capable of binding up to four biotin molecules<sup>7</sup>. The dynamic binding of the biotin to the immobilized SA, shown in Figure 4, was monitored by filling a microplate well with 30  $\mu$ L of PBS, establishing a stable baseline, followed by introduction of 30  $\mu$ L biotin solution (250 ng /mL in PBS buffer solution) into the well. Biotin binding produced a lasing wavelength shift of  $\sim 23$  pm. The biotin solution was also added to sensor wells coated with only proprietary polymer as a negative control, in which no binding signal was observed. For kinetic measurement of an individual sensor without referencing or temperature control, small fluctuations in the ECL wavelength are observed with a magnitude of  $\sim 4$  pm.

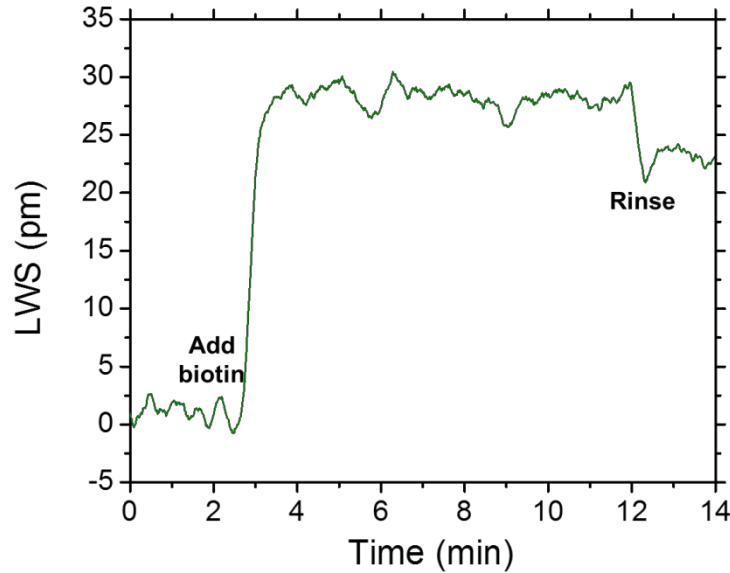


**Fig.4.** Dynamic binding of biotin to streptavidin. Lasing wavelength shift as a function of time during the exposure of a 250ng/mL solution of biotin to the streptavidin-activated sensor.

To demonstrate detection of biomolecular interactions with binding affinities more representative of biological systems, PC surfaces were functionalized with synthetic 20-mer single-strand DNA oligonucleotide probes subsequently exposed to complementary DNA oligonucleotide targets to kinetically monitor the hybridization process. The sensor was monitored continuously during the entire sequence of capture probe immobilization, washing, and hybridization as shown in Figure 5(a). Before introducing DNA capture probes, the sensor surface was functionalized with a high density of GA using the same procedure described for the biotin-SA experiment. After GA functionalization, the sensor microplate well was partially filled with a 30  $\mu$ L saline-sodium citrate (SSC) buffer solution (0.045 M sodium citrate, pH  $\sim$ 7.0, 0.45M NaCl, Sigma–Aldrich) to establish a stable baseline. Immobilization of the DNA capture probes (5'-ATT TCC GCT GGT CGT CTG CA-3') was initiated by addition of 30  $\mu$ L 4  $\mu$ M concentration of the molecule in SSC buffer solution to minimize laser wavelength shift occurring through change in bulk refractive index. As a result, the in-well concentration of the DNA probes is 2  $\mu$ M. At the 5' end of the DNA probes, a tail of 12 amine groups facilitates binding of the DNA to the GA surface via covalent bonds. The sensor was incubated in the probe DNA solution for approximately 60 minutes, allowing the lasing wavelength to saturate at a stable value, followed by rinsing the sensor surface three times with SSC buffer solution to wash off any unbound DNA. In order to prevent the non-specific binding between the target DNA and the GA surface, a blocking step using ethanolamine (EA, 200 mM) was performed to chemically react with any remaining aldehyde groups on immobilized GA molecules. We observed an initial rapid increase in lasing wavelength due to the greater refractive index of the blocking solution, followed by a more

gradual negative wavelength shift during the blocking process, as loosely bound GA molecules and DNA probes were removed from the PC surface. Following a second rinse step in SSC buffer to remove the blocking solution, a stable baseline was established by adding 30  $\mu\text{L}$  SSC buffer solution to the well. 30  $\mu\text{L}$  target single-strand DNA solution with a complementary sequence to the probe DNA (3'-TGC AGA CGA CGA GCG GAA AT-5') was pipetted into the well. For this experiment, six separate biosensor microplate wells were prepared in order to separately evaluate six target DNA concentrations with 3 replicate wells for each concentration. The binding of target DNA was monitored for over one hour, allowing the laser wavelength shift to equilibrate to a new stable value, followed by a third rinse in SSC buffer to remove any unbound DNA. Significantly, the entire sensor preparation, probe immobilization, and target hybridization process was monitored with the smallest increment in laser wavelength shift of 0.08 pm observed. This is a consequence of the low gain ripple of the SOA, and the 2 m length of the external cavity that provides a 0.08 nm gap between allowed modes. A plot of the target DNA binding phase of the process is shown for all the analyte concentrations in Figure 5(b).

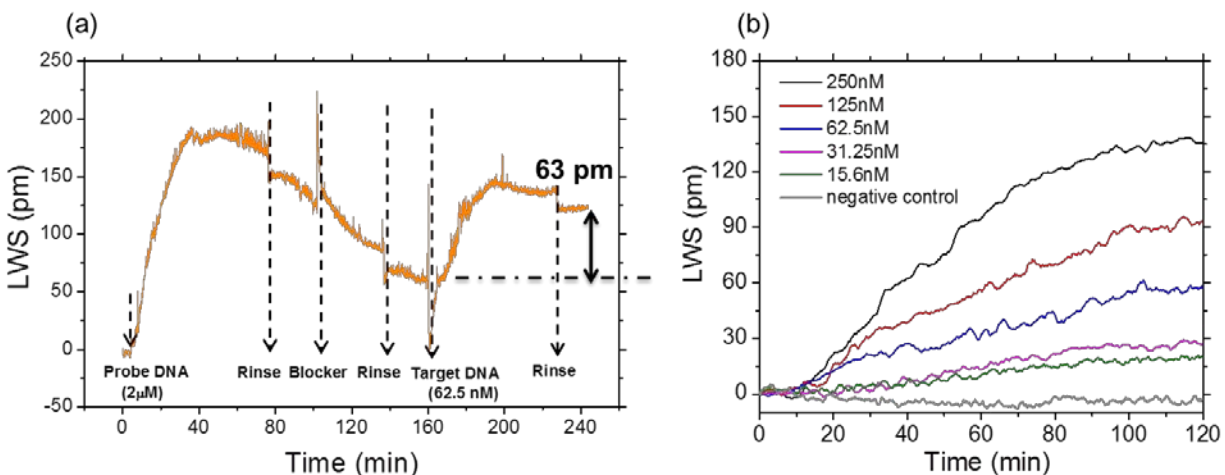


**Figure. 5.** Demonstration of biomolecular interactions with binding affinities more representative of biological systems: Dynamic measurement results of the specific hybridization of complementary probe DNA and target DNA molecules. (a). LWS through the probe DNA immobilization, blocker blocking, and target DNA hybridization and buffer rinsing process. (b) Selection of binding curves with varying target DNA concentrations.

### External cavity laser label-free biosensor based on PC resonator: Future work

In future work, we plan to incorporate effective methods for accurate sensor referencing that will enable this platform to detect small molecule-protein interactions with high signal-to-noise ratio for applications in pharmaceutical high throughput screening. It is also our goal to explore

applications for optical biosensors that are typically challenging, such as direct detection of viral particles and detection of miRNA at low concentrations.

## References:

- 1 Stenberg, E., Persson, B., Roos, H. & Urbaniczky, C. Quantitative Determination of Surface Concentration of Protein with Surface Plasmon Resonance Using Radiolabeled Proteins. *Journal of Colloid and Interface Science* **143**, 513-526 (1991).
- 2 Rich, R. L. & Myszka, D. G. Survey of the year 2007 commercial optical biosensor literature. *Journal of Molecular Recognition* **21**, 355-400, doi:10.1002/jmr.928 (2008).
- 3 Rich, R. L. & Myszka, D. G. Survey of the 2009 commercial optical biosensor literature. *Journal of Molecular Recognition* **24**, 892-914, doi:10.1002/jmr.1138 (2011).
- 4 Ge, C., Lu, M., Zhang, W. & Cunningham, B. T. Distributed feedback laser biosensor incorporating a titanium dioxide nanorod surface. *Applied Physics Letters* **96**, 163702-163703 (2010).
- 5 <http://www.superlumdiodes.com/pdf/soa372.pdf>.
- 6 Lu, M., Choi, S. S., Wagner, C. J., Eden, J. G. & Cunningham, B. T. Label free biosensor incorporating a replica-molded, vertically emitting distributed feedback laser. *Applied Physics Letters* **92**, 261502-261503 (2008).
- 7 Livnah, O., Bayer, E. A., Wilchek, M. & Sussman, J. L. Three-dimensional structures of avidin and the avidin-biotin complex. *Proceedings of the National Academy of Sciences* **90**, 5076-5080 (1993).

## Section 4. Progress Report on Photonic Crystal Enhanced Microscopy

In this progress report, we will show the latest research of photonic crystal enhanced microscopy (PCEM) project. By introducing the PCEM system, we are able to detect the cells without using any kind of dye or fluorescence.

### Introduction to PCEM project

With the rapid development in biotechnology, the demand to accurately detect, measure and characterize the cells has become higher and higher. The traditional method with dye or fluorescence will potentially bring extra influence to the cells, such as modifying analyte conformation, blocking binding sites. Here we use the photonic crystal biosensor to conduct a non-contact accurate detection. And the significant advantage of such sensor is its cheap fabrication cost and easy to be put in mass manufacture. The structure of the biosensor is shown in Fig1.

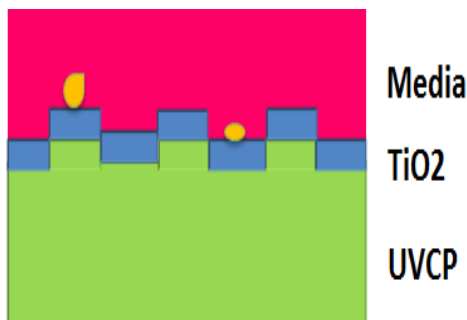


**Fig1.** Biosensor structure. The grating pattern on UV curable polymer is made through replica molding. Then TiO<sub>2</sub> is deposited on the top.

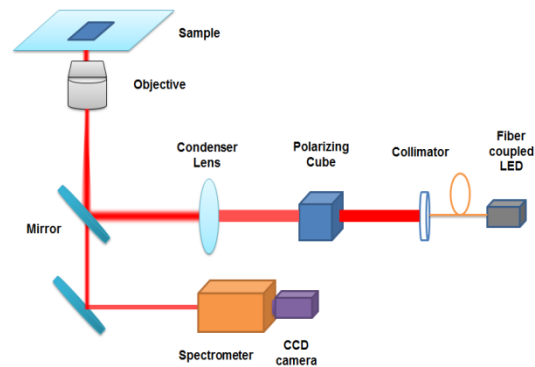


**Fig2.** PCEM system instrument schematic.



## PECM Setup

In the PECM system, the light source is a 620nm fiber coupled LED. After being collimated by the collimator, the light passes through a polarizing cube to provide a transverse magnetic mode. The condenser lens will focus the light into the back focus plan of the objective after the light being reflected. The reflected light from the sample will be received by the CCD camera after passing through a spectrometer. The instrument schematic is shown in Fig2.

## Cell test on the PECM system

The polarized light will induce the guided-mode resonance of the biosensor. And this resonance is sensitivity to the refraction index of the sample we detect. Since the cells have a different refraction index from the media. We can observe such resonance at different peak position. With such kind of peak wavelength value shift, we can get PECM image of the cells. The sensitivity of our sensor is around 100nm/RIU. Besides the good sensitivity, another advantage of the PECM system is that we can observe the motion of the cells since we use such non-contact detects. In Fig3, we show the bright field image and PECM image of cells at T0 and the PECM image at 10 hours later.

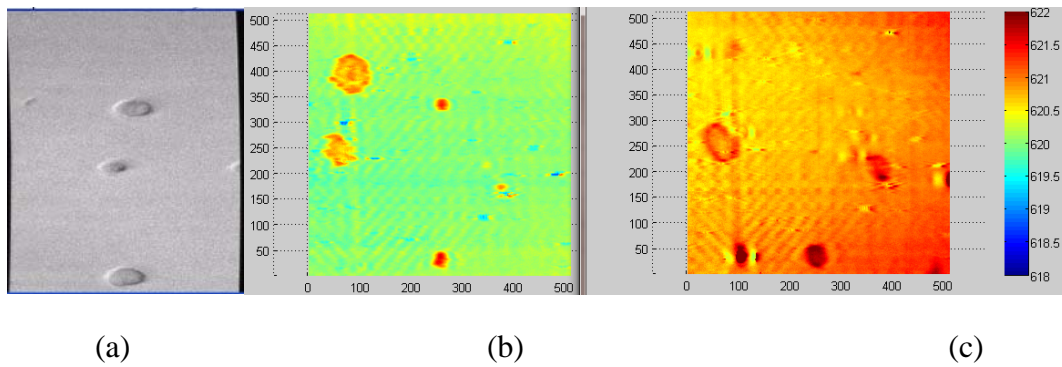


**Fig3.** (a) The bright field image of the cells. (b) PECM image of the cells at T=0 hour. (c) PECM image of the cells at T=10 hours.

## **Summary**

We've displayed the latest research of the PCEM project in Nano Sensors Group. With the designed sensor structure and instruments shown above. We can get the label-free image of living cells at a quite good sensitivity. We are looking forward to use this system to detect the cell attach performance in the future.

## APPENDIX: ARTICLES IN REFEREED JOURNALS

1. EA, Lidstone, V. Chaudhery, A, Kohl, V Chan, T Wolf-Jensen, R Bashir, B.T. Cunningham. "Label-Free Imaging of Cell Attachment with Photonic Crystal Enhanced Microscopy", *Analyst*, 2011, 136 (18), 3608 - 3615
2. EA, Lidstone, V. Chaudhery, A, Kohl, V Chan, T Wolf-Jensen, R Bashir, B.T. Cunningham. Label-free detection of cell-cell signaling between cancer and the immune system, for submission to the *Journal of Biological Chemistry*
3. C. Ge, M. Lu, W. Zhang and B. T. Cunningham, "Distributed feedback laser biosensor incorporating a titanium dioxide nanorod surface", *Applied Physics Letters*, Vol. 96, p.163702, 2010.
4. C. Ge, M. Lu, X. Jian, Y. Tan, and B.T. Cunningham, "Large-area organic distributed feedback laser fabricated by nanoreplica molding and horizontal dipping," *Optics Express*, Vol. 18, Issue 12, p. 12980-12991, 2010.
5. C. Ge, M. Lu, Yafang, Tan and B. T. Cunningham, "Enhancement of pump efficiency of a visible wavelength organic distributed feedback laser by resonant optical pumping", *Optics Express*, Vol. 19, Issue 6, p. 5086-5092, 2011.
6. Y.F. Tan, C.Ge, A. Chu, M. Lu, W. Goldshlag, J. Huang, A. Pokriyal, S. George, B.T. Cunningham, "Plastic-Based Distributed Feedback Laser Biosensors in Microplate Format", *IEEE Sensors*, Vol. 12, Issue 5, p. 1174-1180, 2012.
7. C. Ge, M. Lu, S. George, C. Wagner, J. Zheng, A. pokhriyal J. G. Eden and B. T. Cunningham, "External cavity laser biosensor", *Nature Communications*, under review, May 2012 .
8. J. Zheng#, C.Ge#, C.J. Wagner, M. Lu, B.T. Cunningham, J.D. Hewitt, and J.G. Eden, "Tunable Ring Laser With Internal Injection Seeding and an Optically-Driven Photonic Crystal Reflector", *Optics Express*, Vol. 20, Issue 13, p. 14292-14301 (2012) (# authors contributed to this work equally)
9. Y.F. Tan, C.Ge, A. Chu, M. Lu, W. Goldshlag, J. Huang, A. Pokriyal, S. George, B.T. Cunningham, "Distributed Feedback Laser Biosensor Noise Reduction", *IEEE Sensors*, Vol. 12, Issue 5, p. 1174-1180, 2012.

\*\*\*\*\*